TEKNILLINEN TIEDEKUNTA

Design of an additively manufactured heat exchanger

Sakari Leponiemi

Konetekniikan tutkinto-ohjelma

Diplomityö

11/2022

ABSTRACT

Design of an additively manufactured heat exchanger

Sakari Leponiemi

University of Oulu, Degree Programme of Mechanical Engineering

Master's thesis 2022, 78 pp.

Supervisor(s) at the university: Juho Könnö and Jussi Salakka

The use of additive manufacturing is getting increasingly common in all areas of engineering. In this work, the design of an additively manufactured air-to-water charge air cooler for a 20cm-bore internal combustion engine is studied. This heat exchanger must be capable of 130 kW of heat transfer with 1% pressure loss under tight geometric constrains imposed by the printer bed size. Furthermore, it must be manufactured from a single piece and fit in the cramped space of a laboratory engine intake system. Computational fluid dynamics with the OpenFOAM-suite was used to find a heat exchange surface geometry that meets these requirements. Overall performance estimations and comparisons to conventional tube-fin heat exchangers are made using the ε-NTU-method.

Powder-bed manufacturing methods, like selective laser melting, have advantages for use in heat exchange applications. The high surface roughness and freedom in shape generation are very useful for high performance heat exchange applications. On the other hand, minimum wall-thickness and feature size limitations make conventional heat exchange surfaces, such as finned tubes, somewhat problematic. The use of computational fluid dynamics makes it possible to generate novel heat exchange surfaces that retain the performance of conventional geometries but are well suited for additive manufacturing.

The fundamentals of forced convective heat transfer formed the basis for studying novel geometries: short characteristic length of each individual heat transfer surface and high local flow velocities maximize heat transfer for a given area. Some interesting studies using airfoils as heat transfer surfaces provided the inspiration for a numerical investigation performed in this work. Airfoil tubes proved to be highly effective heat

transfer geometries, matching or exceeding conventional fin-tube surfaces. The use of additive manufacturing allows the design of conformal heat exchanger shapes and the optimization of each tube for the local flow condition.

Computational fluid dynamics was used to find the optimal array of heat exchange tubes. CFD is highly useful when used with additive manufacturing as it can be used to virtually test and optimize a design for highly complex flow conditions, such as those found in turbocharging systems of modern internal combustion engines. If the numerical simulations can be validated by experimentation, additively manufactured heat exchangers can be designed achieve superior performance to conventional heat exchangers, especially when size and shape requirements are considered.

Keywords: heat exchange, additive manufacturing, computational fluid dynamics

TIIVISTELMÄ

Ainetta lisäämällä valmistetun lämmönvaihtimen suunnittelu

Sakari Leponiemi

Oulun yliopisto, konetekniikan tutkinto-ohjelma

Diplomityö 2022, 78 s.

Työn ohjaaja(t) yliopistolla: Juho Könnö ja Jussi Salakka

Ainetta lisäävien valmistumenetelmien käyttö yleistyy jatkuvasti kaikilla insinöörityön alueilla. Tässä diplomityössä tutkitaan ainetta lisäämällä valmistetun ilma-vesi lämmönvaihtimen suunnittelua turboahdetun polttomoottorin imuilman jäähdytyksessä. Tämän lämmönvaihtimen tulee pystyä 130kW lämmönvaihtotehoon 1% painehäviöllä. Suunnittelua rajoittaa geometrisesti vaatimus valmistaa se yhdellä tulostuksella jolloin suurin sallittu koko on valmistuskoneen tulostuspöydän koko. Lämmönvaihtopintojen geometrian suunnittelussa hyödynnettiin tietokoneavusteista virtauslaskentaa (CFD) OpenFOAM-ohjelmistolla.

Metalliosien tulostamisessa käytetyillä jauhepetimenetelmillä on luontaisia etuja lämmönvaihtimien valmistukseen. Menetelmälle tyypillinen suuri pinnankarheus ja vapaus pintojen geometriassa mahdollistavat korkeatehoisten lämmönvaihtopintojen valmistamisen. Toisaalta seinämänpaksuus- ja piirrekokorajoitteet estävät tiettyjen muotojen, kuten ohuiden lamellien, käytön. Perinteiset lämmönvaihtogeometriat eivät siten ole soveltuvia jauhepetimenetelmillä valmistettaviksi, ainakin mikäli tukimateriaalin ja kappaleen jälkikoneistuksen määrä halutaan minimoida. Näiden syiden takia CFD-analyysin käyttö on luontaista uusien, perinteisesti valmistettujen lämmönvaihtimien suorituskykyyn yltävien lämmönvaihtopintojen löytämiseksi.

Konvektiivisen lämmönvaihdon perusperiaatteita noudattaen kävi ilmi, että yksittäisen pinnan pituuden minimointi ja paikallisen virtausnopeuden maksimointi johtaa hyvään suorituskykyyn. Kirjallisuudesta löytyi tutkimuksia, joissa siipiprofiileja käyttettiin lämmönvaihtopintoina. Siipiprofiilit osoittautuivatkin erityisen tehokkaiksi tässä käytössä, jopa ylittäen perinteisten lamellipintojen suorituskyvyn oikeissa olosuhteissa. CFD:n käyttö mahdollistaa lämmönvaihtimen muodon ja jopa yksittäisten

lämmönvaihtopintojen optimoinnin paikallisiin virtausolosuhteisiin, mahdollistaen erinomaisen suorituskyvyn vaikeissakin olosuhteissa, kuten polttomoottorin ahtoilmajärjestelmässä. CFD onkin erityisen hyödyllinen työkalu yhdistettynä ainetta lisääviin valmistusmenetelmiin, koska se mahdollistaa monimutkaisten ja innovatiivisten pintojen tutkimisen halvalla koekappaleisiin verrattuna. Jos simulaatiot kyetään validoimaan testikappaleilla, voidaan ainetta lisääviä valmistusmenetelmiä hyödyntäen suunnitteleman huomattavasti perinteistä pienempiä ja tehokkaampia lämmönvaihtimia.

Asiasanat: lämmönvaihdin, 3D-tulostus, ainetta lisäävät valmistusmenetelmät, tietokoneavusteinen virtauslaskenta

Preface

This thesis work for the Faculty of Technology at the University of Oulu, describing the design of an internal combustion engine charge air cooler, was commissioned by Wärtsilä Finland oy. It was written from autumn of 2021 to autumn of 2022 with the bulk of the simulation work done in summer of 2022 using OpenFOAM v20.06 at the Wärtsilä cluster in Vaasa, Finland. The thesis contains previous and concurrent work done by fellow Wärtsilä employees Mariusz Przybylski and Simone Dorbolo, who both had a critical contribution for the results of this work. The author is also grateful for the assistance of university supervisors Juho Könnö and Jussi Salakka, whose expertise made it possible to navigate the deep waters of writing process.

I would like to especially thank my foreman and supervisor at Wärtsilä, Éric Lendormy, who has been endlessly patient, helpful and inspirational while guiding me through this process and all of my time at Wärtsilä.

Oulu, 09.11.2022

Sakari Leponiemi
Sakari Leponiemi

Table of contents

Symbols and abbreviations

A	surface area
AM	additive manufacturing
C	heat capacity rate
CAC	charge air cooler
c_f	friction coefficient
c_p	specific heat
f	Fanning friction factor
G	flow-stream mass velocity
HX	heat exchanger
h	convective heat transfer coefficient
j	Colburn factor
k	conductive heat transfer coefficient
L	length
Nu	Nusselt number
Pr	Prandtl number
p	pressure
Q	overall heat transfer rate
q	heat flux density, heat transfer rate
Ra	average surface roughness
Re	Reynolds number
r_h	hydraulic radius
St	Stanton number
T	temperature
U	overall heat transfer coefficient
u	flow velocity
W	mass flow rate
x	characteristic length
y	normal distance from a wall
$y+$	dimensionless wall distance

α	thermal diffusivity
ε	heat exchanger effectiveness
λ	free-flow to inlet area ratio
μ	dynamic viscosity
ν	kinematic viscosity
τ	shear stress
ρ	density

1 PROBLEM SPECIFICATION

1.1 Introduction

Charge air cooling is an essential part of modern supercharged internal combustion engines. Traditionally charge air coolers (CAC) are heat exchangers (HX), that have been designed to utilize conventional manufacturing methods and are often selected from off-the-shelf components. The most common type of CAC in use today is the tube-fin type, where cooling fluid, usually water, runs through tubes that have their surface area augmented with thin fins. Charge air flows parallel to these fins, and heat exchange occurs mostly on their surface. This type is proven effective but is limited in geometry by the manufacturing method. Additive manufacturing (AM) technology allows the relatively easy construction of more complex 3D-shapes, and potentially much more effective heat exchanger designs.

In this thesis the possibilities provided by AM is explored in the application of an additional charge air cooler to support the existing fin-tube heat exchanger in a two-stage turbocharged internal combustion engine, the Wärtsilä W6L20CR-DF. It is a 6-cylinder, 20-centimeter bore, inline, four-stroke, two-stage turbocharged research engine used in Wärtsilä's engine laboratory in Vaasa, Finland. A schematic for the charge air system is presented in Figure 1. It features a low-pressure (LP) and a high-pressure (HP) turbochargers, with an intercooler in between them and an aftercooler before the intake air receiver.

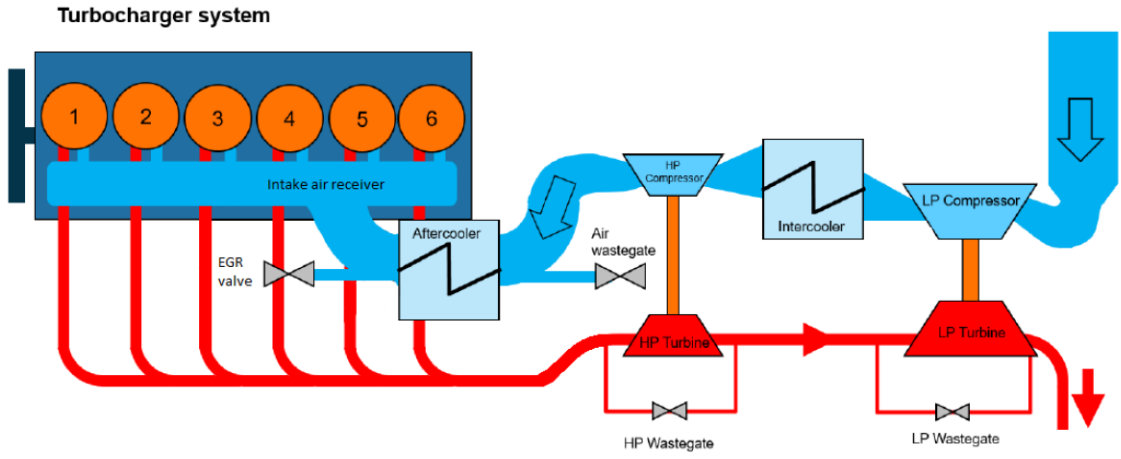

Figure 1. Turbocharger configuration of the W6L20CR-DF.

At 1640 kW engine power, the air engine air mass flow is 2.46 kg/s at 8.73 bar absolute pressure and 343 Kelvin temperature after the HP compressor and aftercooler. This intake air temperature is considered too high, and the goal of this work is to design an additional charge air cooler to support the existing off-the-shelf aftercooler to reach 335 K intake air temperature at under 7 kPa additional pressure loss. The coolant used is water, at 325 K temperature before any cooler. The water mass flow through the additional cooler is not set. The design space is further limited by the geometric constraints of the existing intake piping and structural elements of the engine. Furthermore, the cooler must be able to withstand the high operating pressures and temperatures and varying load conditions of a running engine. The design goal is a single-piece heat exchanger that can be manufactured by selective laser melting (SLM) process and achieves an 8 Kelvin reduction in intake air temperature. Maximum size for the overall heat exchanger is set by the manufacturing process at 29 by 29 by 29 cm. Thus, a high-performance compact heat exchanger is required, so much so that conventional off-the-shelf fin-tube heat exchangers are inapplicable.

The rapid development of available computational power has made the use of numerical methods a valid alternative for traditional experimentation in HX design. Indeed, building and testing prototypes even with modern AM techniques is much slower and more expensive than numerical simulation. Thus, the main design tool for this work is computational fluid dynamics (CFD) using the OpenFOAM-suite. CFD makes it possible to compute the flow field around a geometry at the desired flow conditions and fluid properties, and can include any number of additional phenomena, including heat transfer. The viability estimation of using CFD, and particularly OpenFOAM, for HX design is a key goal of this work.

1.2 Design space limitations and possibilities

The existing engine intake system greatly limits the possible locations of an additional cooler. Only two options are mechanically feasible: a *precooler* between the HP compressor and aftercooler, or a *postcooler* between the aftercooler and the engine itself. As the performance of a heat exchanger is affected by an upstream cooler, a simple calculation of connected heat exchangers was performed to choose between these options. This work was done prior to this thesis by Mariusz Przybylski for Wärtsilä in 2021 (Przybylski 2021). The method used was *number of transfer* units or *NTU,* which will be

described in detail later. The schematic for the heat exchange network is presented in Figure 2. Each heat exchanger is defined in terms of the overall heat transfer coefficient U, heat exchange surface area A, fluid mass flows $\dot{m}$, inlet temperatures T_i and specific heat capacities c_p. From these the overall heat transfer rate Q can be calculated.

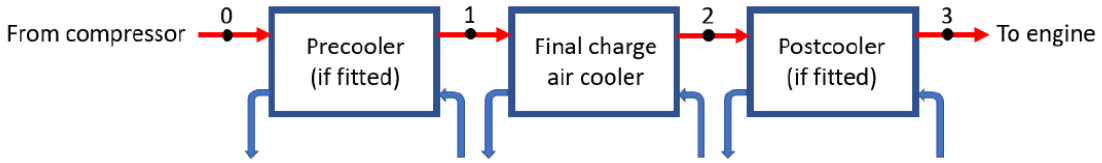

Figure 2. Schematic of the heat exchanger network calculation.

For the calculations, a heat transfer coefficient value of 400 W/m^{2}K was used as an estimate for the pre- and postcoolers. The existing charge air cooler performance is known, so it was modelled with unit surface area as presented in Figure 3.

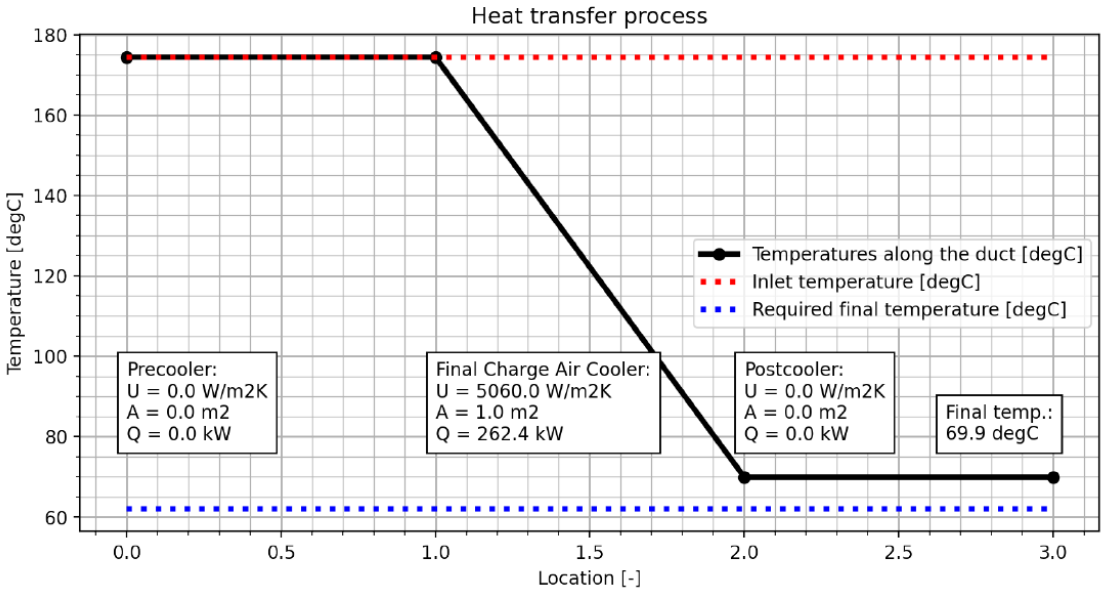

Figure 3. The heat exchange network with only the existing aftercooler installed.

To estimate the impact of an additional cooler, their surface area was varied until the desired final temperature of 62° C (335 K) was reached. The resulting cooler area is 3.775 m^2 for both cases, presented in Figures 4 and 5. While a precooler requires much greater heat transfer rate (140 kW vs 19.9 kW), it can work with much greater temperature difference between the coolant and charge air. Furthermore, a precooler can be designed in a way to improve the inflow conditions of the existing aftercooler, allowing it to operate more effectively. This was not considered in these calculations but will be studied later in this work.

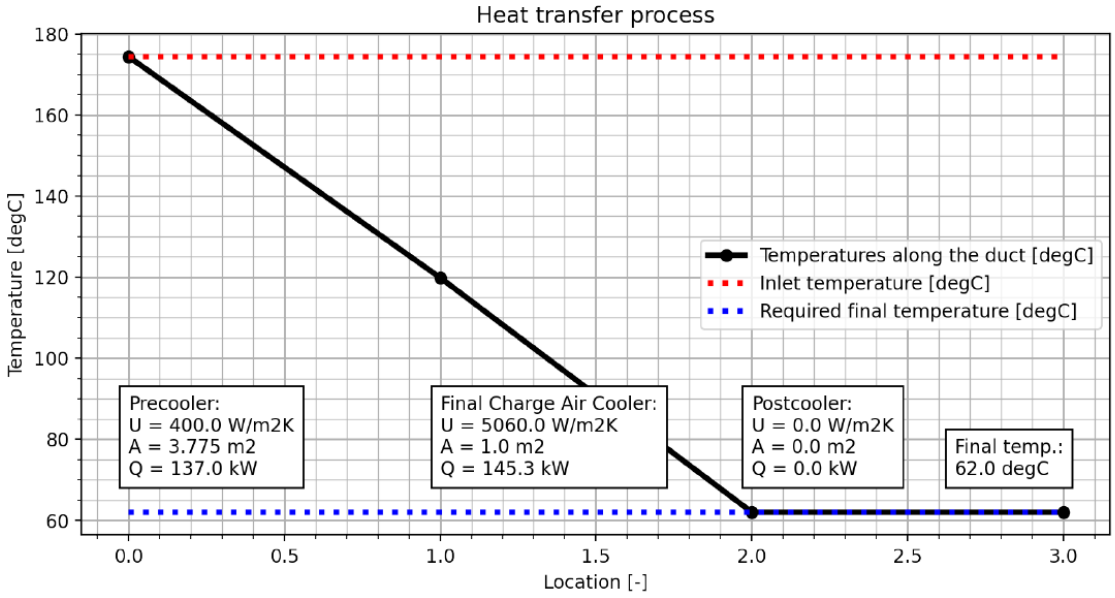

Figure 5. Heat exchange network with a precooler.

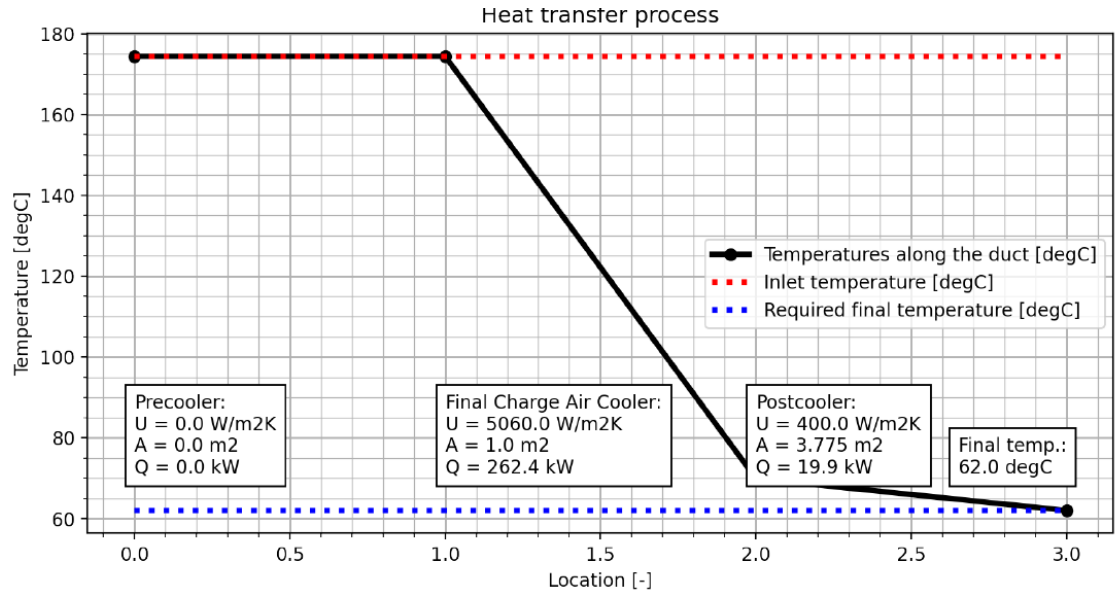

Figure 6. Heat exchange network with a postcooler.

Geometrical constraints on an additional cooler are set by the intake system configuration presented in Figure 7. The HP compressor outlet (grey) and aftercooler (blue) are connected by an intake pipe (green) and funnel (red). The aftercooler is connected to the engine with a collector (white). The charge air cooler and HP turbocharger cannot be moved from their location, limiting the design space available. It was decided that the easiest location for an additional cooler was before the aftercooler, either replacing the intake pipe, funnel or both. Due to these reasons, Przybylski suggests that a precooler configuration should be chosen. The author of this thesis agrees and a postcooler approach will be ignored further in this work.

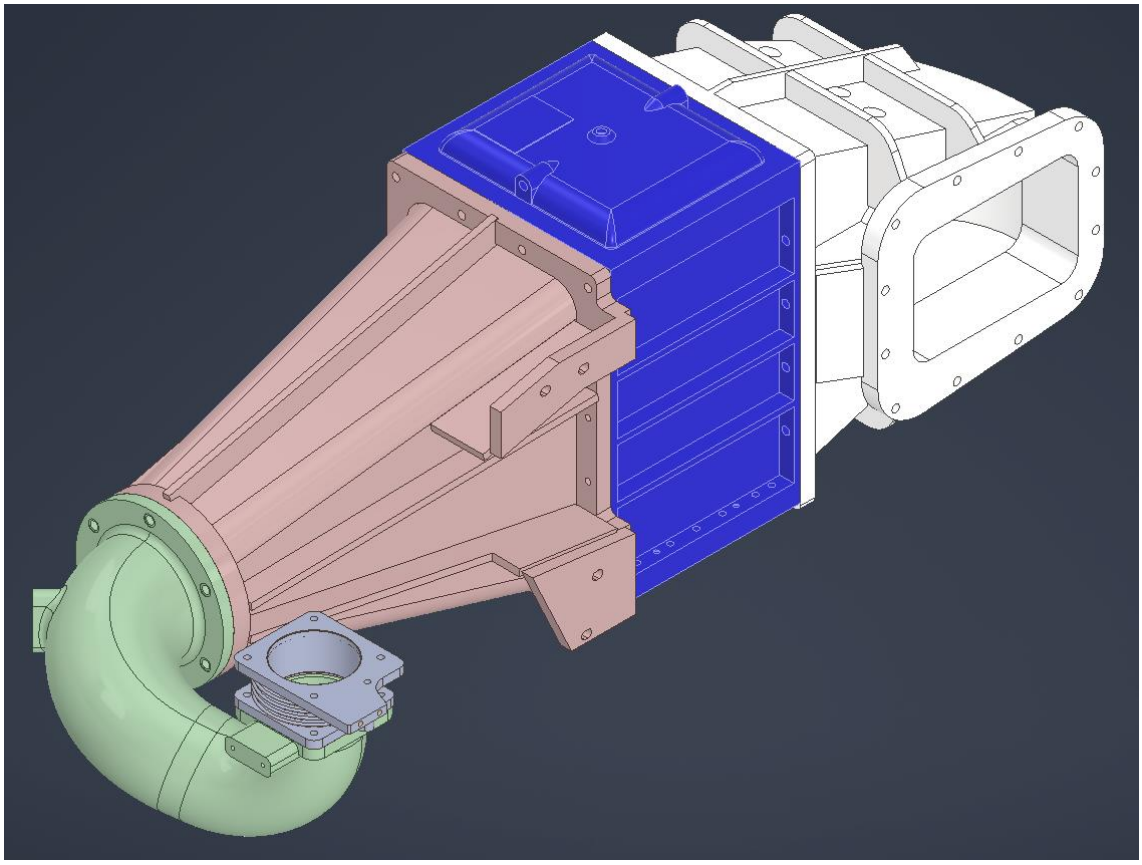

Figure 7. CAD-model of the existing intake air system.

2 MATERIALS AND METHODS

2.1 Basics of heat transfer

Heat transfer is the transfer of thermal energy from one medium to another. As described by the second law of thermodynamics, thermal energy will be transferred from the hotter medium to the colder. This happens via 3 basic mechanisms: *conduction*, *convection* and *radiation*. Thermal radiation, or black body radiation, is the release of thermal energy via electromagnetic waves. It occurs across vacuum or any transparent medium, and all objects emit it due to random movements of particles. Radiation is typically only meaningful in very high energy objects and will be wholly ignored from here on in this work.

Thermal conduction however is of utmost importance for this work. It is defined as the transfer of thermal energy via the interactions of moving particles of matter. Thermal energy flows spontaneously from hot to cold, limited only by the thermal conductivity of the relevant medium. At its most basic form, conduction is described by Fourier's law

$$\mathbf{q} = -k\nabla T, \tag{1}$$

where **q** is the local heat flux density, W/m^2
k is the thermal conductivity of the material, W/mK and
∇T is the temperature gradient, K/m.

From this equation it is easy to derive the basics of heat exchanger design. Maximizing surface area and temperature gradient while using highly conductive materials should yield the best results. However, in applications where one of the mediums is not of high conductance, such as air, the achieved temperature gradient starts quickly limiting the overall heat transfer. The air nearest to the transfer surface equalizes in heat and more heat can only transfer through as conduction through the air. The conductivity of air is several orders of magnitude lower than that of most engineering materials, and so the help of convection is needed.

Thermal convection is defined as the transfer of thermal energy with the medium carrying it. Convection may occur naturally via for example buoyancy effects where heated fluid

changes in density, or it may be forced by inducing flow in the fluid carrying the heat. In most engineering applications, convection is the main mode of heat transfer. Convection is the net effect of both molecular interactions in the medium, known as *diffusion*, and the bulk motion of the fluid, referred to as *advection*. Convection is further divided into *natural convection,* where the change in fluid density drives fluid flow, and *forced convection,* where fluid flow is mainly driven by external factors. For this work, only forced convection is really relevant due to high flow velocities found in ICE intake systems. Effective convection allows the temperature gradient between two mediums to remain high, resulting in high overall heat transfer. Convection can be characterized by Newtons law of cooling

$$\mathbf{q} = h(T_s - T_\infty), \tag{2}$$

where **q** is the local heat flux density, W/m^2

h is the convection heat transfer coefficient W/m^2K

T_s is the surface temperature K and

T_∞ is the fluid temperature in K.

It should be noted that the convection heat transfer coefficient *h* encompasses all modes of heat transfer from the surface to the fluid, including conduction. Thus, the ultimate goal of studying convection is trying to determine *h* (Incropera & DeWitt 1985). *h* is sometimes also referred to *film conductance* due to its dependance on the conditions in the fluid *boundary layer*. The formation of a *velocity boundary layer* is illustrated in Figure 8.

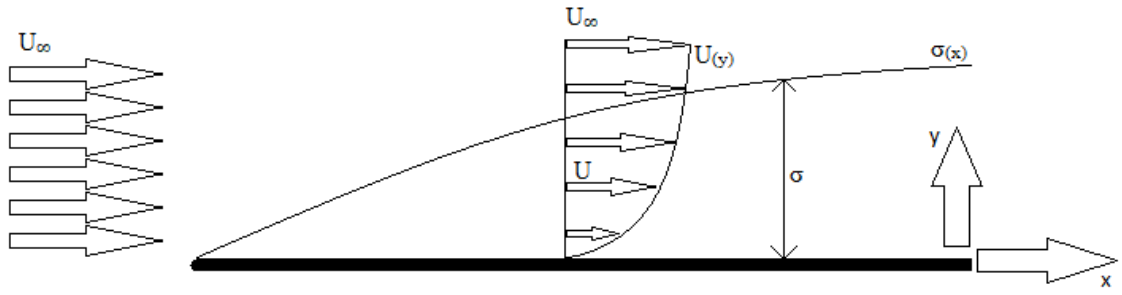

Figure 8. Velocity boundary layer on a flat plate.

2.2 Boundary layers

The boundary layer arises from interaction of a fluid and a surface. *Velocity boundary layer* is the distribution of fluid velocities parallel to the surface: fluid velocity has to be zero at the surface and far away from the surface it reaches *freestream* velocity or U_∞. The thickness of the boundary layer can be defined where flow velocity parallel to the surface $v < 0.99\ U_\infty$ (Incropera & DeWitt 1985). The exact distribution of velocities between these two points is dependent on fluid and surface properties and can be exceptionally difficult to calculate. The surfacewise direction is usually called the x-direction and the direction normal to the surface is called y.

The velocity boundary layer is ultimately caused by friction between the fluid and surface. This friction may be described with the local *friction coefficient*

$$c_f = \tau / \rho u_\infty{}^2, \tag{3}$$

where τ is the surface shear stress,
ρ is the density in kg/m^3 and
u_∞ is the freestream velocity.

The surface shear stress is calculated as

$$\tau = \mu \frac{\partial u}{\partial y}, \tag{4}$$

where τ is the surface shear stress in Pa,
μ is the fluid dynamic viscosity in kg/ms, and
$\frac{\partial u}{\partial y}$ is the local velocity gradient in the surface normal direction in 1/s,

and is thus dependant only on the velocity gradient in the surface-normal direction. The friction factor shows the ratio of wall shear stress to the kinetic energy of the flow per unit volume. It should be noted that τ is possible to accurately define only for very specific geometries and flow conditions, and thus the *apparent* friction factor, also known as the *Fanning friction factor*

$$f_{app} = \Delta p \frac{r_h}{L}, \tag{5}$$

where Δp is the pressure loss through the system in Pa,
r_h is the hydraulic radius of the cooler in m, and
L is the overall flow length through the system,

is used in heat exchanger analysis. This number is much easier to define for a given section, as rh, L and deltaP are all possible to define unambiguously (Shah & Sekulic 2003). Sometimes friction factor is represented with the hydraulic *diameter* as the *Darcy friction factor*

$$f_D = 4f_{app} = \Delta p \frac{D_h}{L}, \tag{6}$$

where D_h is the hydraulic diameter in m.

These friction factors are commonly plotted against the Reynolds number, again to describe different flow conditions. The friction factor is often used to describe the hydraulic performance of a given heat exchanger. A low friction factor value corresponds to low pressure loss in the system. Using a generalized friction factor makes comparisons between geometries possible, at least if they have been tested using the same methodology and conditions.

The velocity boundary layer develops due to difference in fluid and surface velocities, and similarily, a *thermal boundary layer* develops if the fluid and surface temperatures differ. At the surface heat is trasferred only via conduction, as there the local flow velocity is 0. Hence, at y = 0, the heat flux

$$\mathbf{q} = -k\frac{\partial T}{\partial y}\,. \tag{7}$$

where k is the thermal conductivity of the fluid and,
$\frac{\partial T}{\partial y}$ is the temperature gradient in the surface normal direction in K/m.

Combining (2) and (3), we get the *convective heat transfer coefficient*

$$h = \frac{-k\,\partial T/\partial y}{(T_s - T_\infty)}\,, \tag{8}$$

where $T_s - T_\infty$ is the maximum temperature difference between the surface and the fluid.

As k and T_s-T_∞ are constant, the temperature gradient $\partial T/\partial y$ determines the heat transfer rate. As the fluid flows along the surface, heat transfer penetrates further into the freestream. This gives rise to the growth of the thermal boundary layer illustrated in Figure 9: as fluid temperature seeks to equalize with the surface temperature, the temperature gradient $\partial T/\partial y$ must decrease with increase in surface length x. Thermal boundary layer thickness can be defined as the value of y for which the ratio $[(T_s-T_y)/(T_s-T_\infty)]=0.99$. (Incropera & DeWitt 1985)

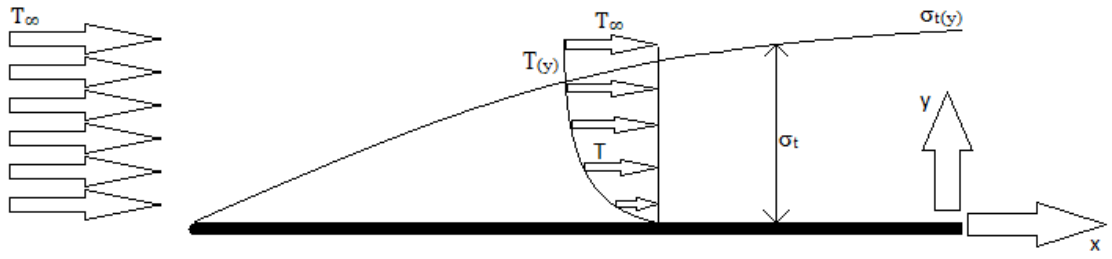

Figure 9. Thermal boundary layer on a flat plate

As flow progresses along a surface, the boundary layer develops not only in thickness, but also in nature: boundary layer may be considered *laminar* or *turbulent*. In laminar flow, fluid motion is ordered and moves along well defined streamlines; in turbulent flow however, the flow is highly irregular and exhibits high velocity fluctuations and spontaneous mixing as shown in Figure 10. This chaotic particle motion enhances transfer of momentum, energy and species in the flow, and thus increases convective heat transfer.

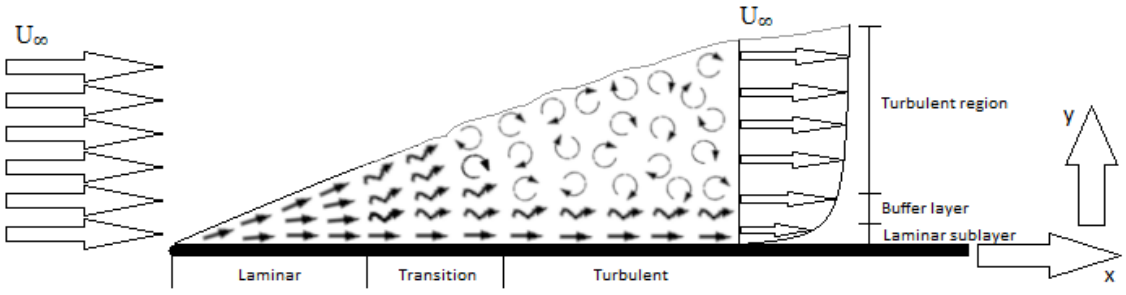

Figure 10. Velocity boundary layer development on a flat plate

A turbulent boundary layer can be further split into three different regions: *laminar sublayer,* in which diffusion is the main mode of tranport and velocity profile is nearly linear; a *buffer layer* where turbulent mixing and diffusion are near equal, and *turbulent layer* where turbulent mixing dominates the transport of properties. The point along the surface (x-direction) where a laminar boundary layer transforms into a turbulent one is commonly described with the *Reynolds number*

$$\mathrm{Re} = \frac{\rho u_\infty x}{\mu}, \tag{9}$$

where ρ is the fluid density in kg/m^3,
u_∞ is the freestream velocity in m/s,
x is the charasteristic length in m and
μ is the dynamic viscosity of the fluid in kg/ms.

For external flows, for example flow along a flat plate, the transition to turbulent boundary layer occurs at Re = 100 000 to Re = 3 000 000, depending on the surface charasteristics, turbulence level of the free stream and the variations of pressure along the surface. The Reynolds number value where turbulent transition happens is called the *critical Reynolds number*.

It should be noted that Reynolds number is dependant on the choice of a charasteristic length. For external flows this measurement is commonly the length of the surface from its leading edge. For internal flows, such as flow in a pipe, this length is usually the *hydraulic diameter* of the pipe. Various formulae exist to calculate this number for different geometries, but this means that Reynolds number is hardly ever defined in an unambiguous manner. For example, in a circular pipe, the Reynolds number for fully turbulent flow is roughly 10 000, at least an order of magnitude *less* than for external flow cases. (Shah & Sekulic 2003, Incropera & DeWitt 1985)

The boundary layer turbulence has a critical effect on heat transfer from a surface into a fluid, especially if the fluid is in gaseous form due to the low conductive heat transfer coefficient of most gases. Inducing turbulence is often desireable in high performance heat exchanger applications as it can greatly increase the overall heat transfer rate. The effects of laminar-turbulent boundary layer transition is illustrated in Figure 11.

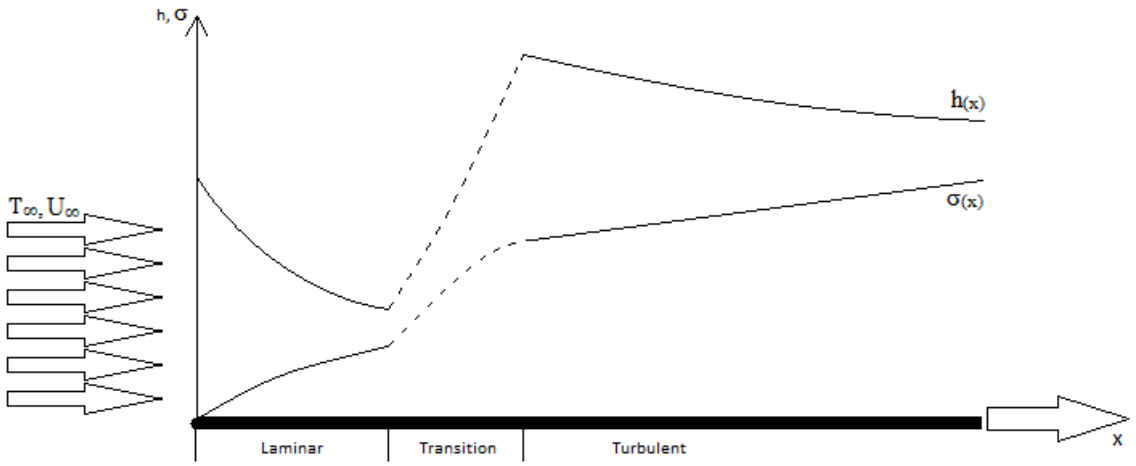

Figure 11. Development of overall heat transfer coefficient h and boundary layer thickness σ over a flat plate.

2.3 Design fundamentals

Some general design principles can be drawn from the fundamentals presented above:

- Materials used should have a high conductive heat transfer coefficient
- Materials used must resist the operating conditions, including high temperature gradients and pressures
- If the working fluids have highly different conductive heat transfer coefficients as is the case here with air and water, the lower conductivity medium should have a higher overall heat transfer area
- Boundary layers of working fluids should be kept as thin as possible
- Temperature difference between working fluids and heat transfer surfaces should be maximized where possible
- Inducing mixing, either via turbulence or otherwise, is beneficial for overall heat transfer but may lead to higher pressure loss
- Higher local flow velocities will increase heat transfer at the cost of surface friction and therefore pressure drop

As stated by Kays & London (1984), compactness by itself leads to high performance in heat exchanger applications. The reason for this can be derived from the principles above. However, there is a risk of inducing overly high pressure loss in the system: it tends to increase as the square of inlet velocity. If mass flow through the system remains constant, inlet and minimum free-flow area determine the flow velocity and therefore overall

volume has a lower limit set by the allowable pressure loss. The design problem then becomes the pursuit of maximum overall heat transfer under this constraint.

2.4 Key parameters groupings

Experimental data for heat exchangers is often presented in dimensionless form to facilitate the vast variety of application geometries. Care should be taken when comparing test data from author to author or even test to test, as the definitions of these parameters may vary significantly. Nonetheless, use of dimensionless groupings is a necessity to establish general trends in heat exchange surface performance.

Minimum free-flow area of a heat exchanger core in m^2

$$A_c = A_{in}\lambda = A_{in}(1 - B)\ , \tag{10}$$

where A_{in} is the core inlet area in m^2
λ is the ratio of HX free-flow area to the inlet area and
B is the *maximum* fraction of inlet area blocked by the core geometry anywhere along its length.

The flow-stream mass velocity is critical when estimating overall HX performance. It can be described as the overall mass flow corrected for blockages presented by a heat exchanger core. It is defined as

$$G = \frac{W}{A_c}\ , \tag{11}$$

where W is the mass flow rate in kg/s.

From the minimum free-flow area we can define the hydraulic radius of a HX core

$$r_h = \frac{A_c}{A} L\ , \tag{12}$$

where L is the overall length of the HX core in the direction of the flow in m and
A is the overall heat transfer area in m^2.

The Reynolds number of a HX core can then be defined:

$$\mathrm{Re} = \frac{4 r_h G}{\mu}. \tag{13}$$

A commonly used nondimensional number used in describing heat exchange surface performance is the relationship between conduction and convection at the boundary layer of a fluid. It is often described using the *Nusselt number*

$$\mathrm{Nu} = \frac{\text{Convective heat transfer}}{\text{Conductive heat transfer}} = \frac{hL}{k}, \tag{14}$$

where h is the convective heat transfer coefficient W/m^{2}K,
L is the charasteristic length, m, and
k is the thermal conductivity of the material, W/mK.

As thermal conductivity is set by the properties of each medium, maximizing convection in the boundary layer increases the overall heat transfer. Thus a high Nusselt number is desireable in many heat exchanger applications. The Nusselt number is also useful because it is relatively easy to measure directly: the thermal conductivity is often well known and convective heat transfer can be measured as the overall heat transfer from a test system.

An important grouping describing fluid properties is the *Prandtl number*

$$\mathrm{Pr} = \frac{\nu}{\alpha} = \frac{\mu/\rho}{k/(c_p \rho)} = \frac{c_p \mu}{k}, \tag{15}$$

Where ν is the momentum diffusivity or kinematic viscosity in m^2/s,
α is the thermal diffusivity in m^2/s,
μ is the dynamic viscosity in kg/ms,
k is the thermal conductivity in W/mK,
c_p is the specific heat in J/kgK and
ρ is the density in kg/m^3.

Prandtl number describes the relationship of momentum and energy transport in a medium. A low Prandtl number fluid for example, such as a liquid metal, exhibits far greater energy than momentum diffusion. For most gases, Pr ~ 1, and for air Pr = 0.7.

A useful combination of these nondimensional numbers is the *Stanton number*, which measures the ratio of heat transfer into a fluid to the thermal capacity of this fluid. Stanton number is defined as

$$\mathrm{St} = \frac{\mathrm{h}}{\rho \mathrm{u} c_\mathrm{p}} = \frac{\mathrm{h}}{\mathrm{G} c_\mathrm{p}} = \frac{\mathrm{Nu}}{\mathrm{RePr}} . \tag{16}$$

The Stanton number is often modified into the *Colburn factor*

$$\mathrm{j} = \mathrm{StPr}^{2/3} . \tag{17}$$

This is done to reduce the Stanton number dependancy of the Prandtl number. As Prandtl number varies according to fluid properties, generalizing it in this way allows it to remain useful for a larger range of working fluids. The Colburn factor is often used to analyze the heat exchange charasteristics of a heat exchanger. It is commonly plotted against the Reynolds number to represent varying flow conditions. (Shah & Sekulic 2003, p. 432-451)

The overall friction factor of of a HX core can be calculated using the geometric data and fluid properties. This definition of friction factor takes into account the exit and entrance losses associated with HX cores and is straightforward to compute from experimental or simulation data. This definition of friction factor will be used for all results presented in this work. (Kays & London (1984) p. 36)

$$\frac{\Delta p}{p_{in}} = \frac{G^2 \nu_{in}}{2 p_{in}} \left[(1 + \lambda^2) \left(\frac{\nu_{out}}{\nu_{in}} - 1 \right) + f \frac{A \nu_m}{A_c \nu_{in}} \right] , \tag{18}$$

where Δp and p_{in} are the pressure loss and inlet pressure in Pa,
ν_{in}, ν_{out} and ν_m are the inlet, outlet and median specific volumes (reciprocal of density) of the fluid in m^3/kg and
f is the dimensionless overall friction factor.

The efficiency of a HX core is often described with the relation of Colburn factor j over friction factor f. For experimental results it is often plotted against the Reynolds number of a particular geometry to describe the behaviour at different flow conditions, however at high Reynolds numbers, ie. fully turbulent flow, the behaviour is expected to converge on some value so experimental data at high Reynolds numbers (> ~15 000) is uncommon.

2.5 Literature review

2.5.1 Overview of AM in HX design

Additive manufacturing is becoming increasingly common in heat exchanger production and its application is being actively researched. AM technology is emerging as a viable alternative to traditional manufacturing methods, offering improved thermal-hydraulic performance and reduction in weight and cost. The main drawbacks seem to lie in mass production and variable product quality. (Kaur & Singh 2021)

The main AM method for metallic HX applications is selective laser melting (SLM) and comparable processes such as direct metal laser sintering (DMLS) and selective laser sintering (SLS). All of these processes are based on a fine-grain metal powder being bonded into shapes by heating the grains with high-intensity lasers. The piece is then built layer by layer by spreading more powder over the previous layer and repeating the process. The final part is usually heat treated after being built to even out residual stresses and ensure low porosity and uniform quality. Commonly available production machines are capable of ~0.5mm minimum feature size and ~45 degrees of unsupported build angle. Lower angles are achievable by building support structures between the part and the bed. Common issues with these methods include high surface roughness, high manufacturing tolerances at small feature sizes and geometry warping due to high thermal stresses. However, a part well-designed for these techniques can be manufactured in a repeatable, reliable and flexible fashion. (Kokkonen et al. 2016)

Kaur & Singh (2021) categorize the many possibilities of AM in HX design as described by Figure 12. Of these fields, some are not applicable to ICE charge air cooling: microchannels and cellular materials exhibit far too large pressure drop characteristics, heat pipes require phase change which is undesirable, turbomachinery cooling is mainly focused on film cooling and internal cooling of turbine components and jet impingement focuses on cooling points on surfaces, which again is not applicable to charge air cooling. Surface roughness and area & turbulence promoters will be discussed here as they are relevant to the goals of this thesis.

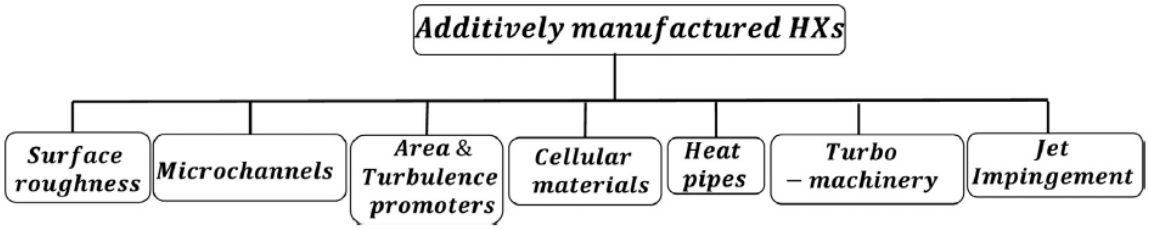

Figure 12. Division of additively manufactured heat exchangers (Kaur & Sing 2021).

2.5.2 Surface roughness

One of the main advantages of AM is the inherently high surface roughness of finished components. Ventola et al. (2014) studied this effect by manufacturing sample surfaces at various orientation angles to the building platform. This study was performed using the DMLS manufacturing process and AlSi10Mg alloy. It was demonstrated that the resulting surface roughness could be controlled with this orientation angle and that increasing surface roughness has a **major positive impact on convective heat transfer performance**. Due to the testing methodology however, surface friction or pressure loss data could not be obtained.

Surface roughness with regards to pressure loss has been widely studied in pipe flow cases, however not so much for AM products. Stimpson et al. (2016) tested DMLS-built microchannels against smooth counterparts and found that pressure losses increase faster than heat transfer, at least when the surface roughness relative to hydraulic diameter is comparatively high. This result is in agreement with pipe flow data from Huang (2012), who found that at high relative roughness (surface roughness/pipe diameter) the friction factor increases faster than what early experimental data would suggest. Stimpson also found that **manufacturing variance becomes high at small (< 0.5mm) feature size, causing significant uncertainty in hydraulic performance**. These small feature sizes are inherent to electronics cooling, which is seen as a major future application for AM heat exchangers. This manufacturing inconsistency is another reason to avoid small feature sizes if possible.

Whilst small scale AM test pieces have been under active study, full scale AM heat exchangers are not commonly represented in the literature. Saltzman et al. (2017) designed and tested an AM aircraft oil cooler against a conventionally manufactured HX of similar design. The HX was a finned tube crossflow unit described in Figure 13, not

too dissimilar to what could be applicable for charge air cooling purposes in this work. The increased surface roughness of the AM unit is clearly observable. Some modifications in the geometry were also necessary to facilitate powder bed fusion (SLM) manufacturing method using AlSi10Mg alloy. At 0.3mm fin thickness, the design was right on the limit of AM capability and some cracks and voids were found in the test pieces. Heat transfer rate however was increased by some 10% over conventionally manufactured units, but the air side pressure drop was roughly doubled. The results from Saltzman et al. are in line with earlier, small-scale experiments and are well explained by the increased surface roughness, especially considering the very high relative roughness of the AM unit. These results also strengthen the view that **small feature sizes and wall thicknesses should be avoided to retain manufacturing quality**.

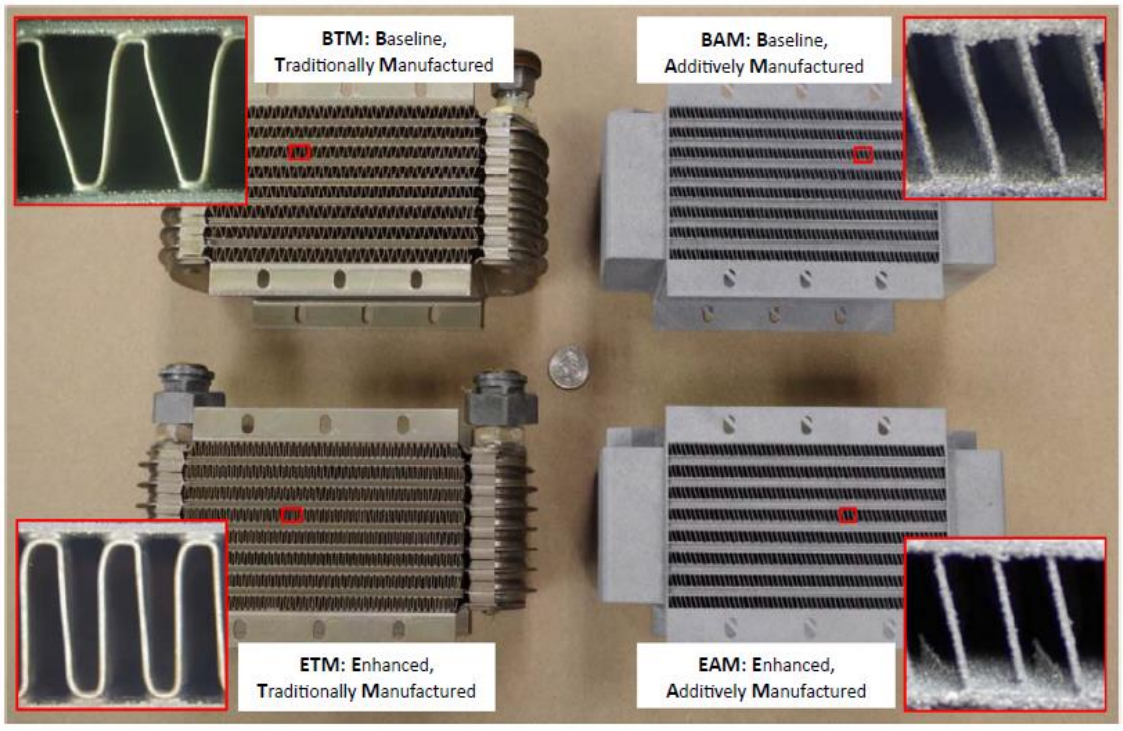

Figure 13. Comparison of conventional and AM heat exchangers (Saltzman et al. 2017).

The common feature with most research on AM HX surfaces is their limitation to small temperature differences, low flow velocities, low Reynolds numbers and low operating pressures. This contrasts with the objectives of this work, where the operating conditions are much more extreme, with over 100K temperature deltas and >7 bar operating pressures. Majority of the studies are also focused on the small feature size capability of AM, which again is not very applicable to the problem at hand. Small features inherently lead to high pressure losses, which is problematic for the scale of a large-bore internal

combustion engine. On average, SLM-built HX surfaces seem to exhibit average surface roughness (Ra) values of 10-25 µm, with even 40 µm being possible with extreme manufacturing angles (Ventola 2014). This roughness is difficult to obtain using traditional manufacturing methods and has consistently proven useful in enhancing heat exchanger performance. Only when flow channel size approaches ~15 times the average surface roughness the pressure losses start to increase rapidly (Huang 2012, Stimpson 2016). This result should not become problematic due to the larger scale and feature size of the HX under design in this work.

2.5.3 Area & turbulence promoters

Perhaps the most interesting possibility AM opens is the capability to manufacture shapes not viable via conventional methods. These geometric possibilities have been under wide study, both as area and turbulence promoters and as cellular materials, such as porous lattice structures as presented in Figure 14. However, the inherently high pressure losses caused by small flow passages in cellular materials makes these structures mostly undesirable for CAC applications. Another problem with lattice structures is their relative inefficiency due to their reliance on secondary cooling surfaces (Wong et al. 2009, Al-Ketan et al. 2020), and their applications seem to mostly lie in electronics cooling and structural uses instead of forced convection cases such as the one presented here (Kaur & Singh 2021).

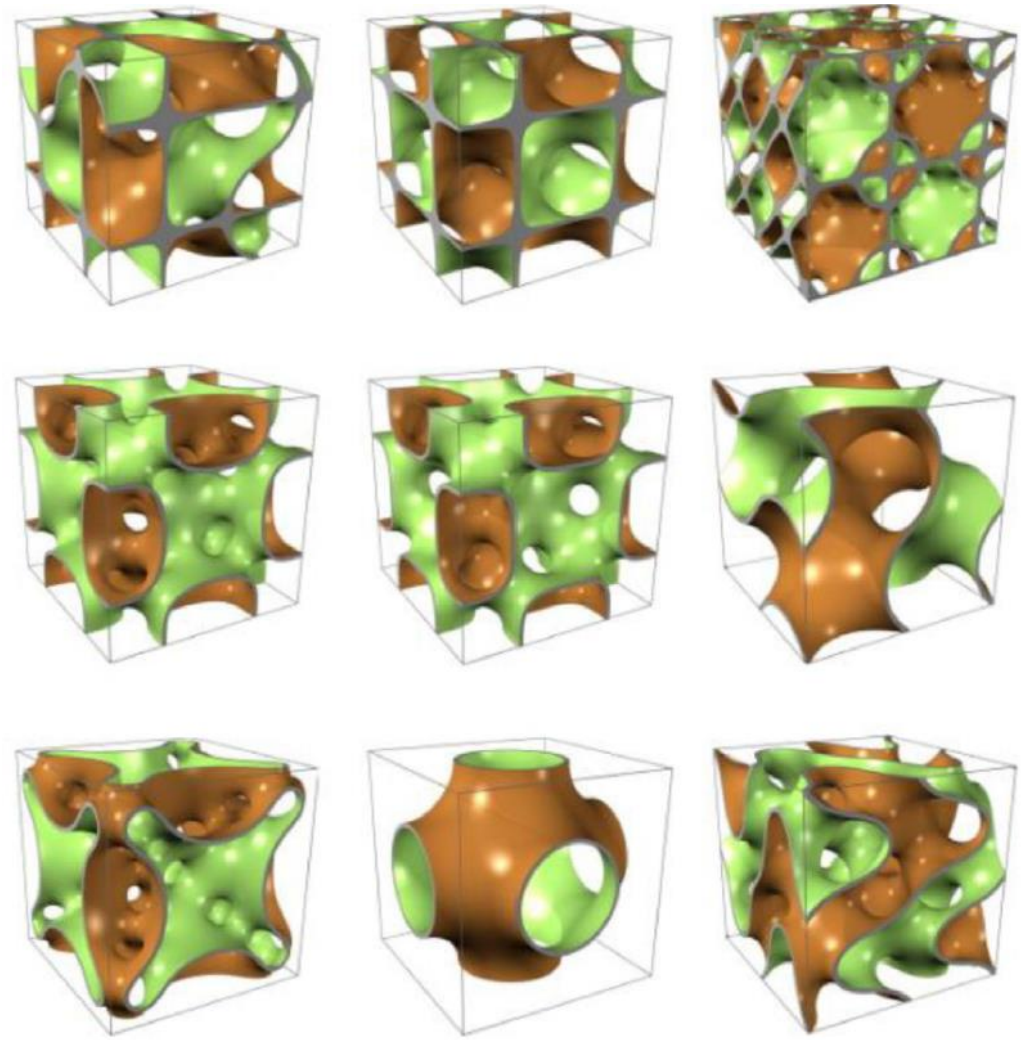

Figure 14. Examples of cellular material topologies made possible by additive manufacturing (Kaur & Singh 2021).

More relevant to a CAC application are vortex generators. An example of so-called chevron-type vortex generators is shown in Figure 15. Important early work on vortex generators and heat transfer was summarized by Fiebig (1998). He makes a distinction between transverse vortices, such as the famous Karman vortex street, and longitudinal vortices which have their axis in the flow direction. These longitudinal vortices may provide significant increases in heat transfer due to the increased turbulence and rotational mixing. Transverse vortices on the other hand seem to have a negligible effect on heat transfer. As summarized by Fiebig (1998), heat transfer provided by vortex generators is maximized with an angle of attack around 45 degrees, and height of up to half the flow channel height and 6 times the boundary layer thickness. Triangular and rectangular winglets appear to give similar performance, other parameters being equal.

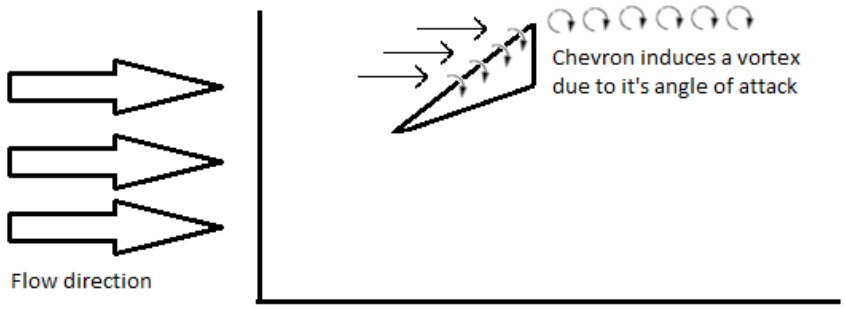

Figure 15. Schematic of a chevron-type vortex generator.

Rastan et al. (2020) studied the application of vortex generators in AM minichannel heat exchanger. It was found that best geometries could produce up to three times the convective heat transfer as compared to smooth channels. The study was, however, done using water as the test fluid at low Reynolds number (170-1380). This laminar flow regime is far from the conditions in an ICE CAC, but the results demonstrate the feasibility of using vortex generators in AM applications. The pressure loss was very high, but this can partly be explained by the otherwise laminar flow of the test system. Rastan et al. (2020) also demonstrated the feasibility of using numerical simulation to predict heat transfer augmentation of vortex generators, achieving good correlation between their numerical and experimental models.

While vortex generators are meant to augment the function of an existing surface at small feature sizes, AM allows the realization of large-scale surface geometries not available to conventional manufacturing methods, some examples of which are presented in Figure 16. Wong et al. (2009) studied various SLM-manufactured 6061-aluminium heat sinks, including circular, rectangular and elliptical pin fins and a 3D-lattice structure using a controlled test assembly. It was found that the **elliptical pin array provided highest heat transfer rate per unit pressure drop**, even though the lattice structure had significantly higher heat transfer area. Design optimization or comparison to conventionally manufactured was not included in the work.

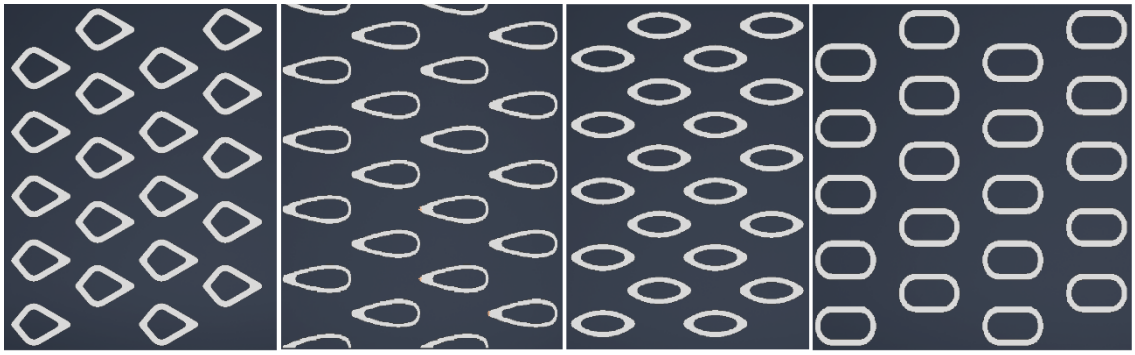

Figure 16. Examples of novel heat exchange surface geometries attainable via AM.

Ho et al. (2017) investigated using NACA airfoils at varying angles of attack as heat exchange surfaces. Several prototypes were built using SLM-methods and tested against a typical circular-fin heat sink. All tested **airfoil surfaces performed better than the baseline heat sinks**. Furthermore, increasing the angle of attack further enhanced the heat transfer, while the exact geometry of the airfoil had minimal effect. In a surprise result, a **rounded rectangular fin shape provided the highest heat transfer rate of all, outperforming even the airfoils**. It was postulated that this was due to higher vortex formation of the rectangular fins' trailing edges. The airfoil shapes provided less flow separation and thus reduced mixing as compared to more blunt trailing edges. Pressure loss data was not obtained due to the testing methodology. Also, the Reynolds number regime was once more quite limited (<24 000), but the advantages of heat transfer surface geometry optimization was clearly demonstrated.

Bacellar et al. (2017) took this approach a step further with a numerical optimization of HX core geometry. Their work argues that **at small tube diameters, secondary surfaces, i.e. conventional fins become unattractive**. Despite the increase in surface area gained with secondary surfaces, finless tubes achieve higher thermal-hydraulic performance. This is postulated to be mainly due to the greater contribution of primary surfaces to overall area density at smaller tube diameters. **Finless designs also naturally exhibit higher convection heat transfer coefficients due to higher local temperature differentials**. Furthermore, with an optimized tube geometry, significant performance increases are achievable. Bacellar et al. (2017) found that, at least numerically, all their optimized tube shapes (which closely resemble airfoils) could achieve the same heat transfer as a tested baseline finned HX, while reducing pressure drop and overall size by more than 20%. The finless airfoil-tube design was validated experimentally by comparing a baseline airfoil tube design against a conventional finned microchannel HX. Their experimental results correlated well with data from CFD, although the test regime

was quite narrow in flow velocities and heat loads. Significant pressure loss and material volume reductions were achieved.

This result is remarkable for AM HX applications, as these novel tube shapes are easily manufacturable by SLM methods. In conventional HX design, fins are often considered a necessity to increase area density of a given core as the primary surface area is quite limited due to ease of using circular coolant tubes. **Thin fins are not easy to manufacture using SLM**, as demonstrated by Stimpson et al. (2016) and later Saltzman et al. (2018). If the use of thin secondary surfaces and other small can be avoided while retaining HX performance, AM techniques become very attractive. Additive manufacturing also opens the door for HX geometries designed around the flow conditions of each particular use case. This type of design should yield further advantages in packaging, material usage and even thermal-hydraulic performance.

2.6 Conventional HX design methodology

Traditionally heat exchangers have been designed using experimental data for common flow- and geometrical configurations. This data is then used in equations for each type to try and determine the correct HX properties for the application. A way of classifying HX:s by their flow arrangement is presented in Figure 17. Other classifications include surface compactness, construction and heat transfer mechanisms.

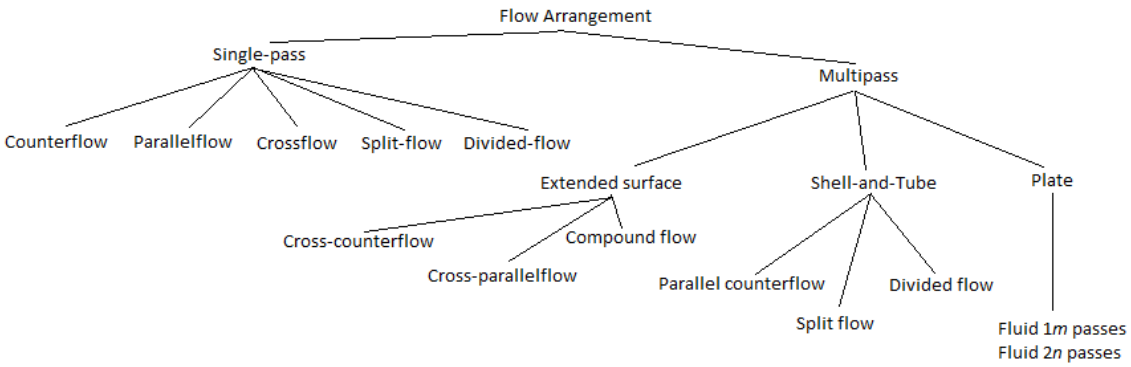

Figure 17. Classification of HX: s according to their flow arrangement.

The reason for classification is empirical. It is not possible to describe all possible variations of geometries and flow conditions analytically. To match experimental data, a set of equations and correlation factors have been established for each of these (and other) idealized cases. Experimental performance data for various common geometries is

tabulated and presented in graph form, allowing designers to *size* and *rate* their heat exchanger design without expensive experimentation. This has been the basis of heat exchanger design since at least the 1950's. (Kays & London 1984 p. 1-48)

According to Kays & London (1984), the problem of heat exchanger design can be split into 2 problem specifications: the rating problem and the sizing problem. The rating problem asks, what is the heat transfer rate and resulting temperatures of a given HX core geometry and flow conditions; the sizing problem is the attempt of optimally sizing the HX core, given certain flow rates and temperatures. This division helps the designer, as the design is usually constricted by the usable design space, reducing the problem of HX design to mostly rating or sizing. Furthermore, once a certain flow arrangement and/or HX construction type is chosen, experimental data is readily available for most common geometries. Often the designer does not get to choose the working fluids, flow arrangement or HX type, but instead it is forced by the application. It is also the case for this thesis work.

2.6.1 ε-NTU example

The ε-NTU method is a common method of solving the rating and sizing problems of a heat exchanger. A typical rating problem of a known HX geometry is solved using the following steps (Kays & London 1984):

1. Find the surface characteristics of the heat exchanger (Eq. 10, 11 and 12)
2. Find fluid properties
3. Compute the Reynolds numbers (Eq. 13)
4. Find the friction and Colburn factors from empirical data
5. Calculate overall heat transfer coefficient using geometrical and thermohydraulic data and appropriate empirical correction factors and equations (for example fouling and fin effectiveness)
6. Calculate number of transfer units NTU and overall effectiveness ε (Eq. 19)
7. Calculate outlet temperatures from overall effectiveness and energy balance
8. Calculate pressure drops (Eq. 18)

NTU or number of transfer units is a nondimensional representation of the "heat transfer size" of a heat exchanger. It is defined as

$$\mathrm{NTU} = \frac{\mathrm{AU}}{\mathrm{C_{min}}}, \tag{19}$$

where A is the overall heat transfer area in m^2,
U is the average overall heat transfer coefficient in W/m^2K, and
C_{min} is the lower heat capacity rate in W/K.

The heat capacity rates C_{min} and C_{max} are calculated as

$$\mathrm{C}_i = W_\mathrm{i}\,\mathrm{c}_{\mathrm{p},i}, \tag{20}$$

where W_i is the mass flow rate of the fluid in kg/s and
$c_{p,i}$ is the heat capacity of the fluid in W/kgK.

Overall heat exchanger effectiveness

$$\varepsilon = \frac{\mathrm{q}}{\mathrm{q_{max}}} = \frac{\mathrm{C_h}(\mathrm{t_{h,in}} - \mathrm{t_{h,out}})}{\mathrm{C_{min}}(\mathrm{t_{h,in}} - \mathrm{t_{c,out}})}, \tag{21}$$

where q and q_{max} are the overall and maximum possible heat transfer rates in W
C_h and C_{min} are the hot fluid and minimum heat capacity rates in W/K, and
$t_{h,in} - t_{h,out}$ is the hot fluid inlet and outlet temperature difference in K, and
$t_{h,in} - t_{c,out}$ is the overall maximum temperature difference in K.

ε and NTU are related to one another using equations appropriate for the flow arrangement of a heat exchanger (counterflow, crossflow etc). Therefore the overall heat transfer rate q can be found if the inlet and outlet temperatures, mass flow rates and fluid properties are known or NTU can be calculated. As NTU is dependant on the overall heat transfer coefficient U, it is always based on existing empirical data. The availability of this data for given flow conditions places a fundamental limit on the viability of this and other methods. These analytical methods will give accurate predictions for HX performance, if:

- There is empirical data available for the chosen heat exchange surface geometry
- Surface and fluid properties match the empirical test setup or are within known correction factor range
- In- and outflow conditions are uniform or easily predictable.

This means that there exists a separation between designing and testing heat exchange *surfaces* and full heat exchangers. Indeed, accurate analytical solutions for heat transfer are only possible for certain simple cases such as laminar flow in a circular pipe. Due to the vast number of possible HX configurations and use cases, manufacturing and testing full heat exchangers for every use case would be costly and impractical. This is where modern numerical methods can significantly improve HX design. 3D-CFD has become increasingly available and been proven to show good agreement with experimental data with various geometries if the computational grid and selected models are appropriate for the use (Aslam Bhutta et al. 2012).

2.7 Design targets for this work

Because the design goal of this work is to create a new heat exchanger with novel surfaces within a volume and inlet area boundary, both the rating and sizing problems need to be solved. Surface-geometrical and thermo-hydraulic data for the HX will be estimated using 3D-CFD, but the design targets can be set using the ε-NTU methodology presented above with some engineering judgment to fill the gaps. The invariant input data for all possible designs is presented in table 1. As the final cooler will operate in laboratory conditions and a lot of pumping power is readily available, the inlet water mass flow and pressure loss can be ignored for now. After the airside performance has been established, it can be mapped for various water mass flows to find an acceptable compromise.

Table 1. Factors that remain constant for all possible designs.

Inlet temperature	Air	447 K
	Water	325 K
Outlet temperature	Air	393 K
	Water	TBD
Inlet pressure	Air	870 kPa
	Water	TBD
Allowable airside pressure loss	Absolute	7 kPa
	Percentage	1 %
Airside mass flow W		2.46 kg/s
Airside heat capacity rate C_{min}		~2660 W/K
Required overall heat transfer rate q		137 kW
Overall required HX effectiveness ε		0.4

As the overall shape and size of the precooler can be chosen freely within the geometric constraints of the intake system, a baseline design space with 20cm circular inlet and 29cm flow-wise length was chosen. This baseline makes it possible to set targets for the surface and thermohydraulic properties of any analyzed heat exchange surface geometry. These targets are presented in table 2. It should be noted that due to modeling uncertainties the target pressure loss and overall heat transfer rate was set at 5 kPa and 140 kW respectively. The surface area density was set at 270 m^2/m^3, as this was considered achievable with the intended manufacturing method. Expected HX blockage was set at 0.45. While each of these assumptions represent a design variable by themselves and offer a range of possible targets, this set of values was considered reasonable and achievable after studying possible HX surface geometries in CAD.

Table 2. Target thermohydraulic properties of precooler airside heat exchange surface.

Inlet velocity	11.6 m/s
Mass flow velocity G	142.8 kgm^2/s
Heat exchanger overall volume	911 cm^3
Overall heat exchange area A	2.46 m^2
Resultant Reynolds number Re	~55 000
Required heat transfer coefficient U	467 W/m^2K
Required power density	15.4 W/cm^3
Required friction factor f	0.0243
Required Colburn factor j	0.0026
Required j/f	0.107

Even when accounting for a small range for all variables, it is apparent that a particularly low-friction surface geometry is required. Empirical data from Kays & London (1984) suggests that only some finned tube geometries reach the required friction factor at high Reynolds numbers, but they fall significantly short of the required heat transfer due to inefficiency of their fins. Bare tubes, circular or flattened, that can reach the required Colburn factor but exhibit far too much friction at the required power density. Thus, novel heat exchange surfaces are required to reach the target, or the design space must be widened, by for example allowing more pressure loss, increasing the intake flow area or lengthening the available HX length.

2.8 Methodology

Computational fluid dynamics, or CFD, is a numerical analysis tool to analyse and solve fluid flow problems. It is based on discretizing the governing equations to make them solvable for cases otherwise impossible. Additional modelling equations, for example for sub-grid scale turbulence phenomena and chemical reactions, can be implemented to simulate a vast array of engineering problems. The end product of this discretization is a system of ordinary differential equations which can then be solved using appropriate solvers. Accuracy of the results depends on the models used, convergence of the iterative solvers but first and foremost the resolution and quality of discretization. As each additional discrete cell adds to the computational effort, and complex geometries with small feature sizes seen in HX applications require a large number of cells to model, full-scale HX CFD-modelling is usually impractical. Estimating the characteristics of HX surfaces in small sections in a manner not dissimilar from old-school experimentation is however reasonably effortless. Results from these simulations can then be implemented in well-proven HX design methods to estimate the performance of novel heat exchanger geometries.

2.8.1 Heat exchange surface simulations

Extensive simulation work was carried out to estimate the performance of novel heat exchange surface geometries. The software used was OpenFOAM v2006 with the *chtMultiRegionFoam* -solver. This solver is a transient compressible solver designed for heat exchange applications in multi-region domains and allows the simultaneous solving of conjugate heat transfer in the solid parts and fluid dynamics in the fluid part. The solver setup is described in detail in table 3.

Table 3. Simulation setup for HX core sections

Solver	chtMultiRegionFoam
Discretization schemes	2nd order "Gauss Gamma 1.0" or "Gauss linear"
Turbulence modelling	k-Omega SST with 3% inlet intensity
Temporal modelling	Euler scheme, adjustable timestep with Courant number < 1, ran until steady-state
Air thermodynamics	Single specie perfect gas at constant viscosity and Prandtl number

Heat capacity and viscosity	Air: 1009 J/kgK and 20.1 μNs/m^2 Solid: 846 J/kgK
Thermal conductivity coefficient	Air: Calculated from other properties Solid 173
Temperature and pressure	Air: 447 K at the inlet, 870325 Pa at the outlet Solid: 325 K at the inner wall

Due to the large physical size of the full HX, simulations were carried out in sections from which performance parameters were extracted. These sections were setup as rectangular tunnels with symmetry boundaries enforced on all sides apart from the inlet and outlet. The inlet provides constant flow velocity, temperature and turbulence properties. Outlet is set at a constant pressure. A typical computational grid is presented in Figure 18.

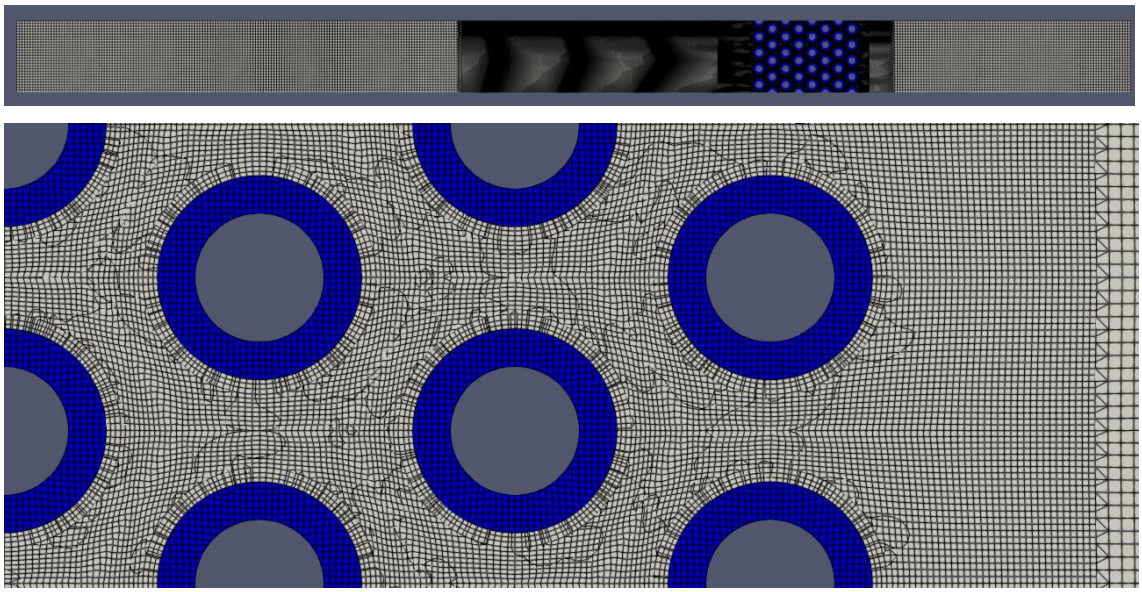

Figure 18. Overview and detail of a computational grid with the solid region in blue and fluid region in white, flow direction is right to left and grid resolution is 0.3mm^3.

Turbulence modelling was performed using the k-omega SST-model in high-Reynolds formulation to reduce overall grid size. The y+ -values were monitored for each simulation and results were discarded if average through the domain was under 30 to ensure correct wall function performance. This was especially critical as the *nutkRoughWallFunction* was used to estimate the effect of surface roughness: it can only be considered valid at y+ >30 and roughness of Ra < 25 μm, so this placed constraints on the range of grid quality, inlet velocity and surface roughness. In practice, this limitation

meant that inlet flow velocities under 5 m/s were not studied. As the expected flow velocities are in the 10-20 m/s range, this was considered acceptable.

Temperature gradient is enforced by setting the inside wall of the solid surfaces at a constant temperature. This simplification is done to remove the need to mesh and solve the water side of the heat exchanger. The water side mass flow and thus temperature distribution is unknown and is the subject of further work, however the water side heat capacity rate is much higher than on the air side and the solid wall thicknesses low and near constant, so this simplification should not present a large source of inaccuracy.

2.8.2 Model verification

To validate the simulation setup, a set of simulations were performed replicating the test methodology and geometry used by Kays & London (1984). They studied numerous HX surface geometries experimentally and detailed their setup, which was replicated here for the circular, smooth surface pin grid case S1.5-1.25. Unfortunately, due to the low Reynolds number limit of their data, only valid comparisons can be made for the case at Re=15 000. As their result data was given in nondimensional form, the core flow length, inlet area and flow velocity were deduced from their Reynolds number definition. The heat exchange and pressure loss data were then converted to the same nondimensional form and is presented in table 4 alongside the original test results, along with comparison to cases computed with increased surface roughness. (Kays & London 1984, p. 152-191)

Table 4. Comparison between experimental and simulation data for flow normal to banks of tubes.

Case	Friction factor f	Colburn factor j
Experimental data	0.0503	0.00690
Simulated smooth tubes	0.0245	0.0037
Simulated tubes at Ra=$12.5 \cdot 10^{-6}$ m	0.0533	0.0045
Simulated rough tubes at Ra=$25 \cdot 10^{-6}$ m	0.0671	0.0048

The chosen simulation method seems to be underpredicting heat transfer, even at high surface roughness, while friction predictions are quite close at reasonable surface roughness. This could be explained by the different test conditions for experimental data: they were tested at atmospheric pressure whereas the simulation had to be run at 8 bar to retain $y+ > 30$ with the available meshing tools. Another explanation is that even though

flow behaviour of any heat exchange surface should converge asymptotically to some value when Reynolds number increases, but the experimental data is often cut off before that point happens. Thus, the high Reynolds number behaviour is unclear in this data. A third explanation is the lack of detail in describing the used experimental methods, for example the number of tube banks and the distance of tubes from outer walls of the flow duct. Also, the tubes used for experimentation may not have been perfectly smooth, causing another factor of uncertainty.

To fully validate and develop the simulation methods, a new set of test data is required, preferably with a known, simple geometry and at the exact operating conditions that a HX is being developed for. While the effort required for this is prohibitive for every possible use case, it could be an option for a large company like Wärtsilä who could have many applications at these operating conditions. The precooler developed in this work should be the first step towards this validation process, as its performance can be measured in the laboratory at any condition provided by the engine. As of writing, this data does not exist and thus simulation results should only be compared with one another within this work, and large margins of error remain for any performance parameter.

3 RESULTS

3.1 Airfoil-tube design

From very early on in the design process it was apparent that a low-friction surface geometry was required to meet the pressure loss goals. After establishing the heat transfer properties of these surfaces, area density could be increased to the limit allowed by pressure loss estimations to reach maximum overall heat transfer. This could be done by increasing the number or area of primary cooling surfaces (surfaces that are in contact with both working fluids) or by the addition of secondary surfaces (these contact only 1 working fluid, for example fins in a conventional HX).

Although AM allows for almost limitless complexity and freedom in 3D-design, some practical limitations remain:

- Wall thicknesses < 1mm should be avoided to avoid cracking and other defects
- Unsupported surfaces at high angles to the build platform must be avoided to prevent the need of support material removal
- Water channel dimensions must be high enough to prevent blockages from possible fouling over extended use. 3mm was considered sufficient for now, although further work is needed on the subject
- Minimum overall feature size should be > 0.8 mm to retain manufacturing accuracy and repeatability

From these limitations a minimum size airfoil shape was designed, as presented in Figure 19. The shape is based on symmetrical GOE776-airfoil with the trailing edge rounded to 0.8 mm. It features overall thickness of 25% at 30% chord length and is comparable to many other catalogued symmetrical airfoils. The thickness of the airfoil allows for a 3mm wide water passage with 1mm wall thickness if the chord length is 18mm. Other airfoil shapes or a novel, optimized shape could be advantageous but as demonstrated by Ho et al. (2017) and Bacellar et al. (2017), the exact shape of the airfoil is not necessarily of critical importance. Any proper airfoil shape should outperform circular or other conventional HX surface shapes in pressure loss characteristics, while retaining the ability to work in non-zero angles of attack unlike flat plates. These airfoils were then arranged

in a matrix and their lateral (cyan) and longitudinal (red) pitch was varied to investigate the importance of their spacing.

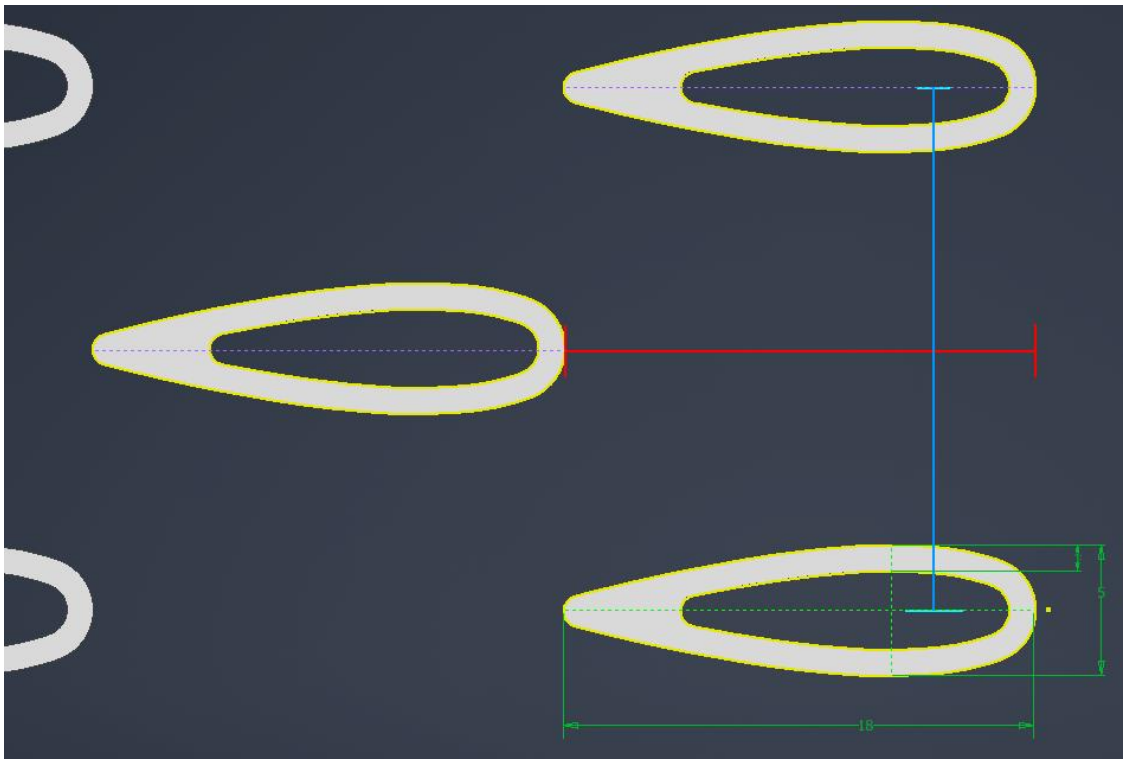

Figure 19. Sizing and arranging of the modified airfoils for studying effects of their spacing.

When comparing these airfoil tubes to typical cylindrical arrays, they perform very differently. At similar area density of 180 m^2/m^3, the airfoil tubes exhibit less than **a fifth** of the pressure drop of a baseline circular tube array, at the cost of approximately halved power density. The reasons for this vastly different performance characteristics can be seen in Figure 20. The circular geometries exhibit heavy flow separation after each tube, vastly reducing the effective flow area of the geometry and causing high fluctuations in flow velocity: the **maximum velocity in the round tube array is roughly 2 times higher than for the airfoil tubes, despite having 85% of the nominal free flow area of the airfoil array.** Round tube arrays still retain high heat transfer rate due to high flow velocities and mixing caused by flow separation. Thus, round tube geometries can offer high heat transfer coefficients and power density, but they become more and more inefficient as the dimensions shrink. If airfoil arrays can provide the required power density, round tube geometries cannot compete with them due to their vastly inferior pressure loss behaviour.

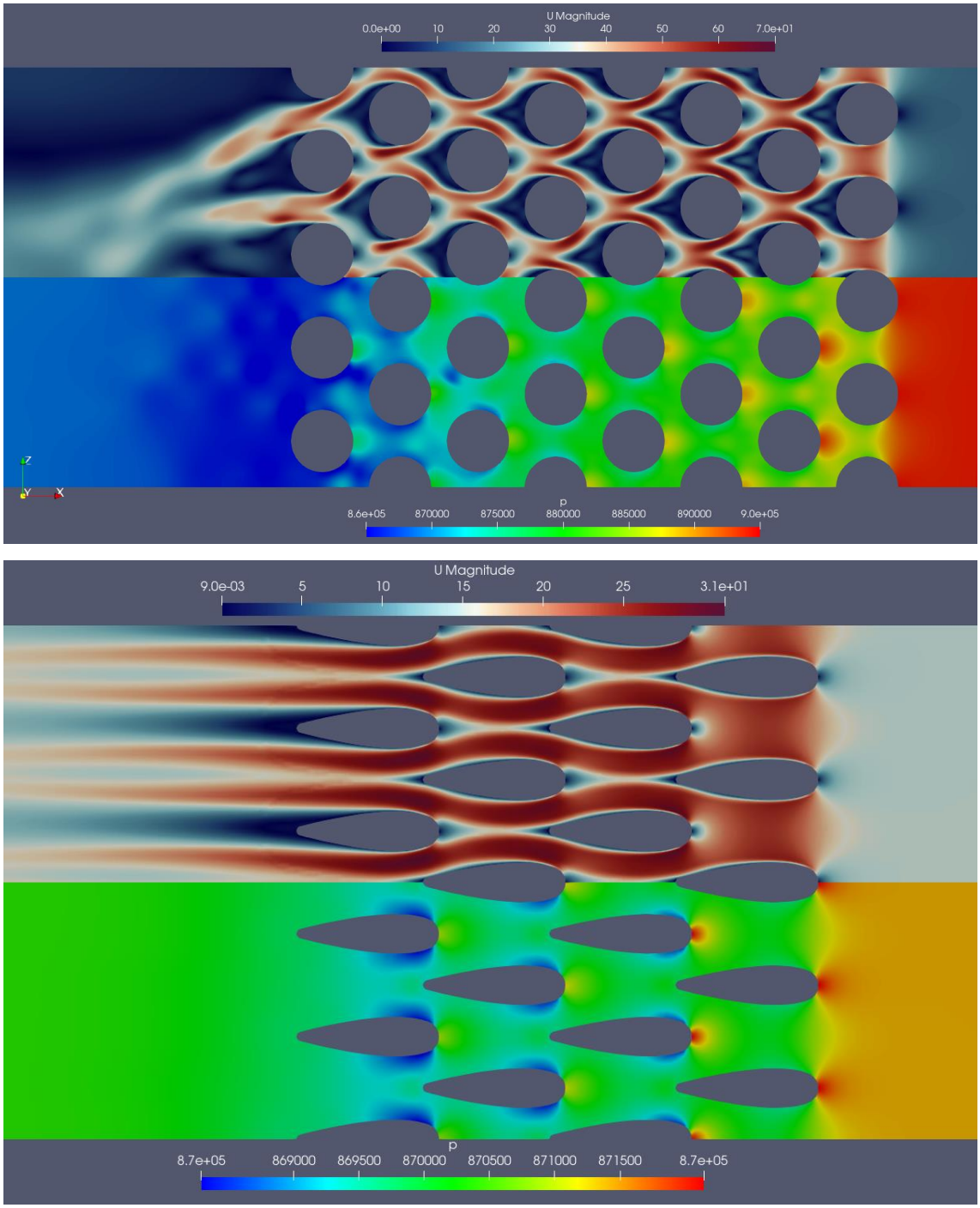

Figure 20. Flow field comparison between circular and airfoil arrays at equal area density with velocity (blue-white-red) and pressure (blue-green-red) fields visualized.

3.1.1 Effect of airfoil tube spacing

The spacing or *pitch* of airfoil tubes has a significant effect on their performance, as can be seen in Figures 21, 22 and 23. Especially notable is the high efficiency shown by the airfoil tubes, despite their lower power and area density, they exhibit much lower friction resulting in high heat transfer for pressure loss (j/f). For longitudinal pitch, the performance peaks at roughly 18mm, which happens to be the chord length of each

individual tube. Whether this remains true for all airfoil shapes and flow conditions was not investigated for now.

At high longitudinal separation, the next row no longer guides flow over the trailing edge of the previous row, resulting in early flow separation and reduced performance as can be seen in Figure 24. Low flow velocities at the trailing edge reduce the heat transfer effectiveness of each fin so much that the increased mixing provided by the flow separation is not enough to offset it. Furthermore, reducing the longitudinal pitch reduces the area and power density, meaning that high tube separation is not desirable in the first place. It should be noted that the highly symmetrical and orderly behaviour seen in Figure 24 is caused due to the uniform intake conditions, but the overall phenomena should apply in real-life situations as well.

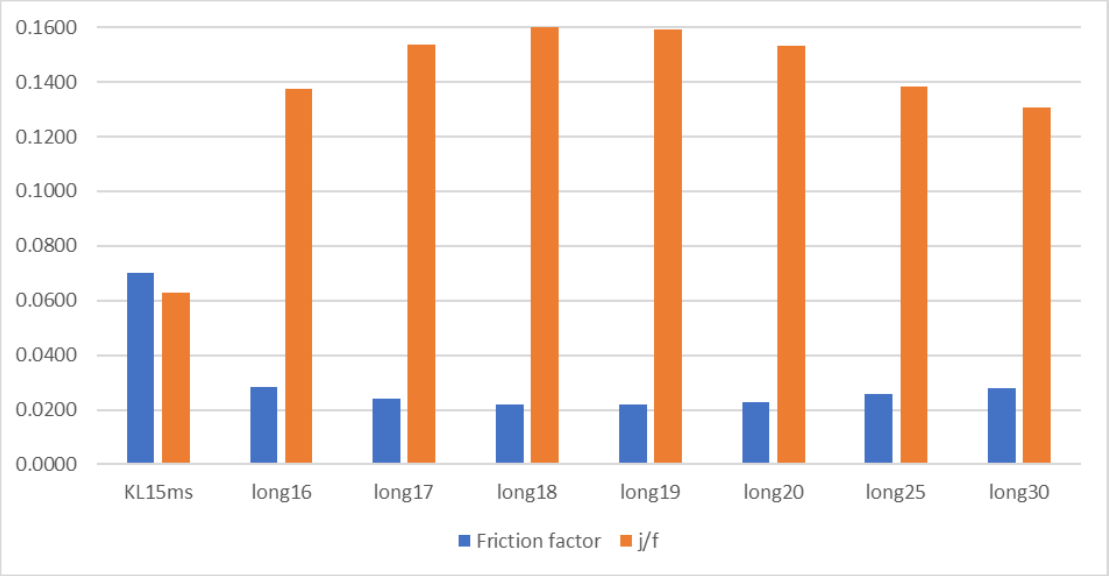

Figure 21. Effect of longitudinal spacing (16-30mm) on core performance at fixed lateral spacing of 10mm, with comparison to Kays & London reference case (KL15ms).

Lateral spacing has much less effect on the performance of each tube apart from reducing the blockage for the airflow and therefore reducing the average flow velocity. Naturally the area and power densities decrease with increasing lateral pitch, as will overall pressure loss due to the higher free flow to inlet area ratio. As all of the studied lateral pitch cases demonstrate similar flow behaviour, it can be said that **longitudinal pitch is the key factor for airfoil-tube HX performance**. Lateral pitch should still be minimized to increase power density as much as is possible given the pressure loss constraints. Lateral pitch can therefore be used as an adjustment tool for a HX design: power density can be traded for overall pressure loss without losing efficiency.

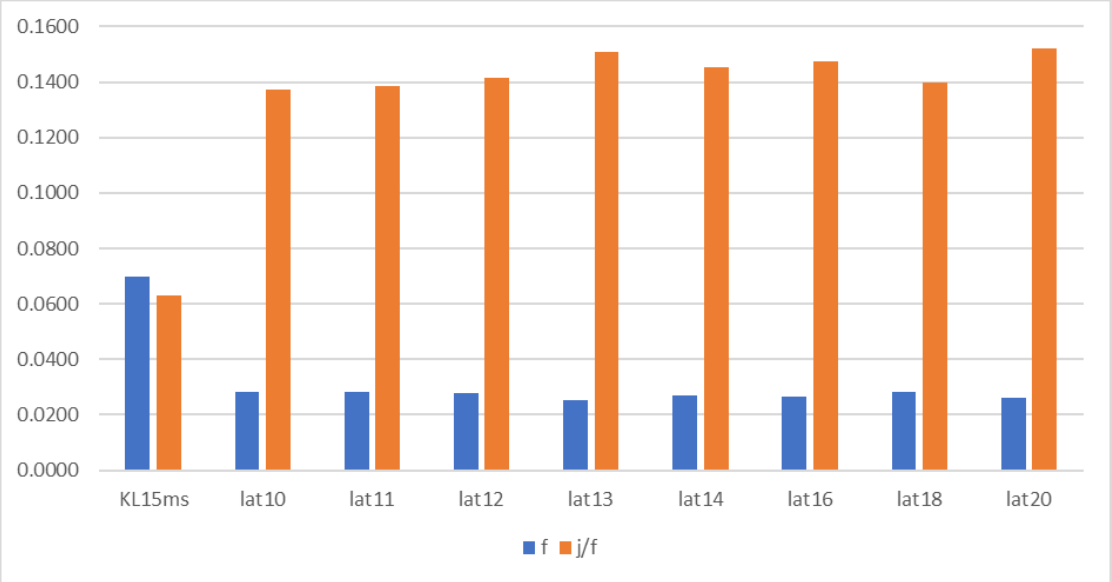

Figure 22. Effect of lateral spacing (10-20mm) at fixed longitudinal spacing of 16mm.

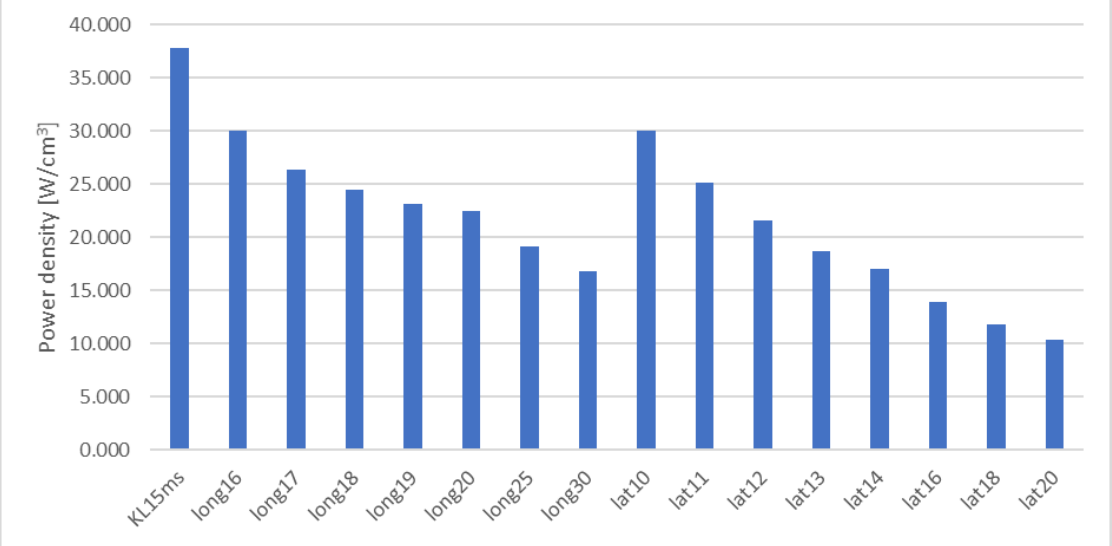

Figure 23. Effect of lateral and longitudinal spacing of tubes on core power density.

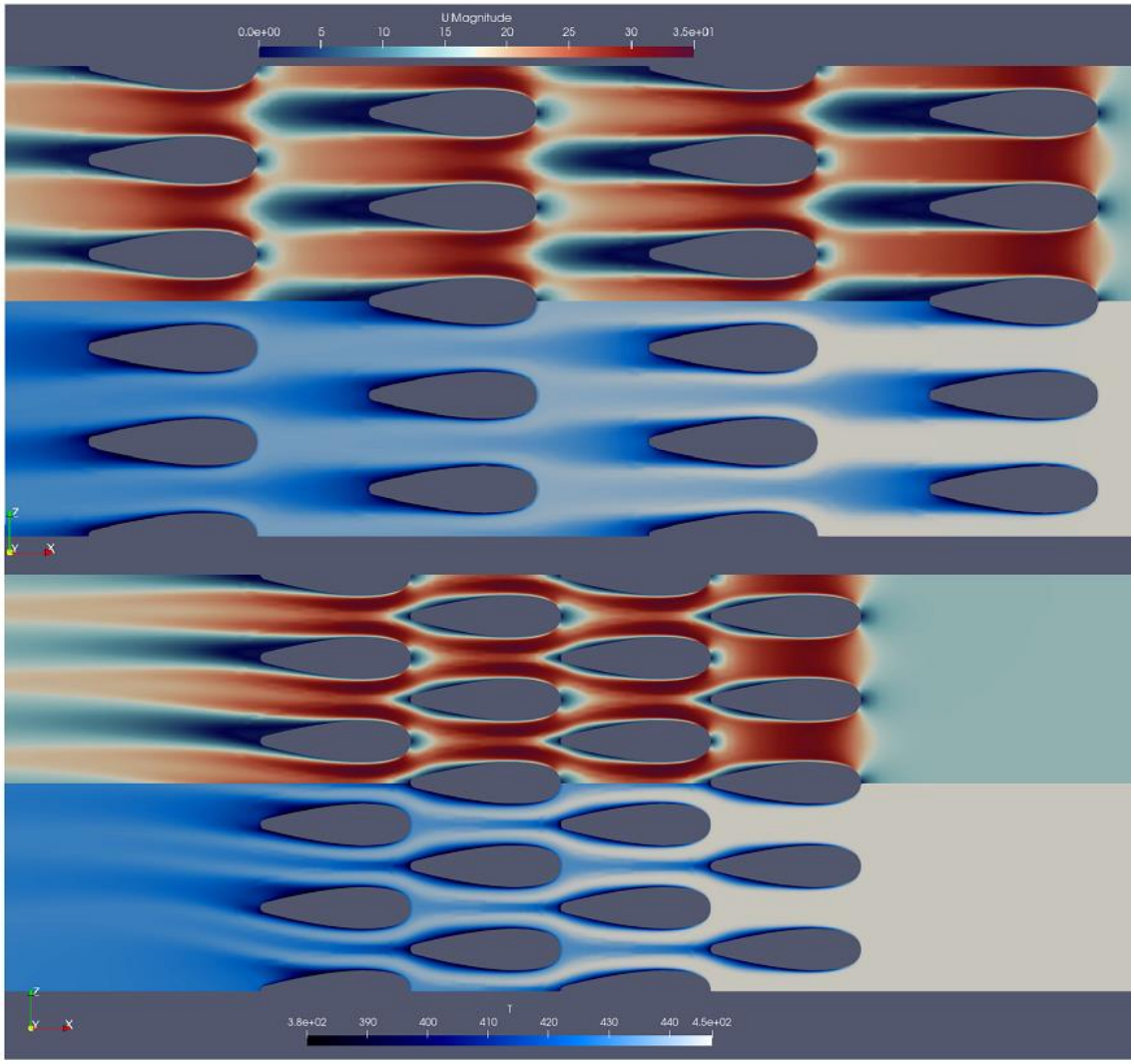

Figure 24. 30mm and 18mm longitudinal pitch cases with velocity (black-blue-red) and temperature (black-blue-white) fields visualized for each.

3.1.2 Tube staggering

Early flow separation and resulting low velocity and low temperature region behind high-pitch tubes inspired an idea of staggering each row of tubes, demonstrated in Figure 25. This staggering moves the next row of tubes away from the "shadow" cast by the previous row. This could have a positive effect on heat transfer, because the boundary layer around a tube is formed by the flow trailing from the tube ahead. If the tubes are staggered, each row should have faster, less turbulent and hotter air to form its boundary layer from, resulting in higher temperature gradient and therefore more heat transfer.

Staggering can be done in several ways. Here it was chosen to stagger the tubes by choosing a row count n, and then moving each row by **lateral pitch/*n* (or pitch*2/*n* at *n* > 4)**. This method of staggering ensures that there remains a sufficient gap between

adjacent rows' trailing and leading edges. The issue with this method is the need for high lateral pitch: unless there is sufficient separation between the tubes, the trailing and leading edges of adjacent rows will interfere with each other. This kind of staggering also leads to "directionality" in the tube arrays as can be seen in Figure 25. This could be countered by for example mirroring the staggering across the center flow-wise axis, but some directionality will alwas presist with staggered tubes. Tube staggering can also lead to geometrical issues near the outside walls of an array. This happens because the rows are no longer spaced evenly from the outside wall, leading to "cut" tubes or very small gaps between a tube and the wall. These issues are not insurmountable but demand additional care from the designer.

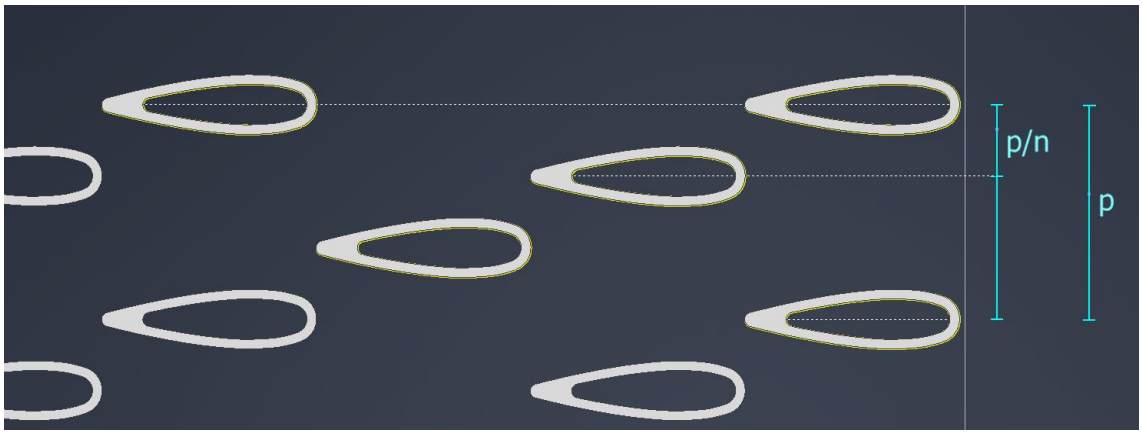

Figure 25. Staggering of tubes by row count n, here $n = 3$.

As seen in Figure 26, tube staggering does not result in any gain in efficiency. Staggered arrays even exhibit slightly higher friction factors, most likely due to their irregular behaviour near the domain walls, as seen in Figure 27. While this is an artefact of the chosen simulation method, it also represents a very real design challenge of staggered tube arrays near HX core outside walls. Staggered arrays do perform slightly better in heat transfer, but this is not enough to offset the friction losses and the extra complexity caused by staggered arrays. Figures 27 and 28 show the effect of tube staggering: air cooled by previous row does not influence the next row as much as in non-staggered cases. In Figure 28, a method to counter array directionality was tested: moving the rows in sets of 2. This case, named *nonDir* in Figure 26, performed the best but was still unable to beat the baseline non-staggered array for efficiency. It can be assumed that other tube geometries, like round and oval tubes, exhibit similar design issues if staggered similarly. Another staggering method should be employed if any real gains are to be found, but this route was not pursued further in this work, as **the gains from tube staggering are**

negligible at best, reduce the overall area and power density and require significantly more design effort if implemented in a full-scale heat exchanger.

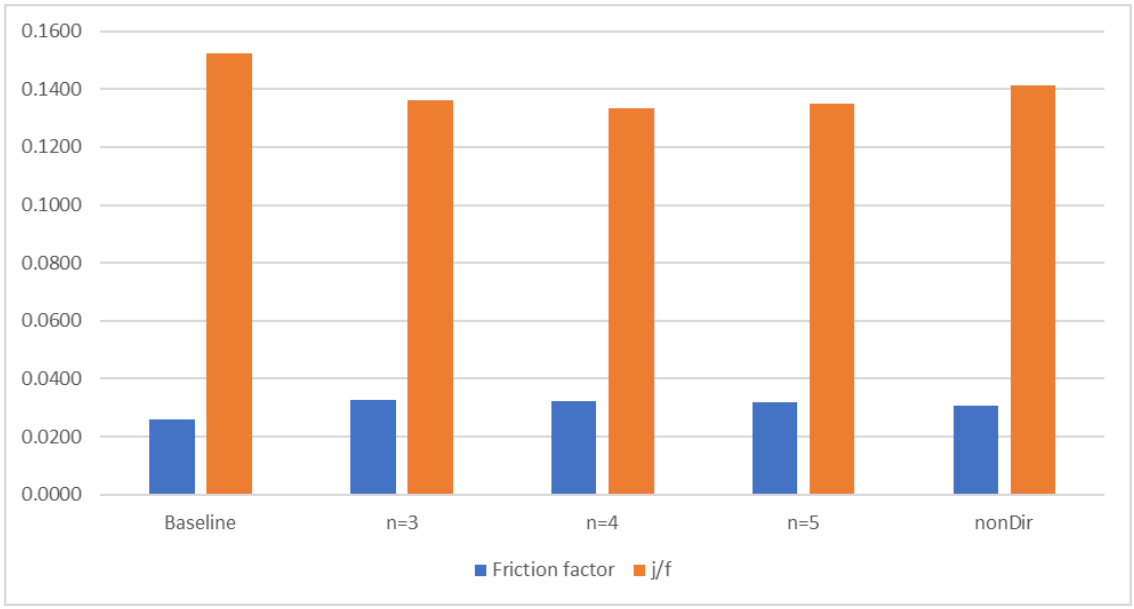

Figure 26. Performance characteristics of staggered arrays compared to baseline array with similar lateral and longitudinal pitch.

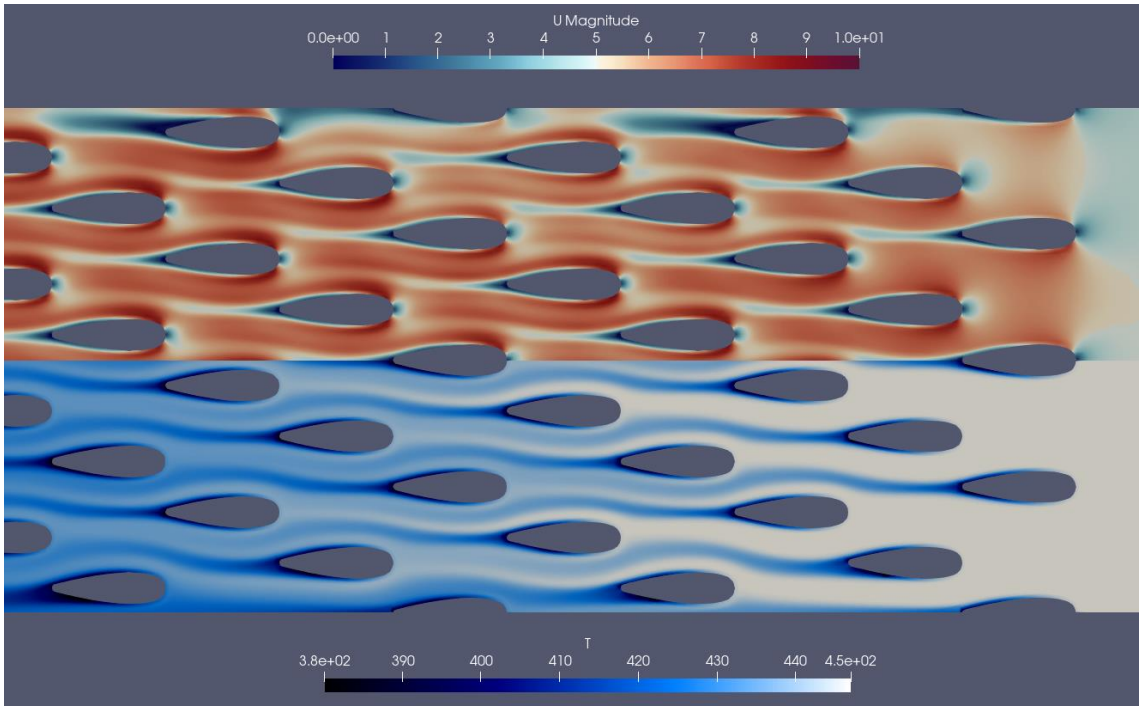

Figure 27. Flow field around staggered airfoil tubes at $n = 5$, velocity field (black-blue red) and temperature field (black-blue-white) visualized.

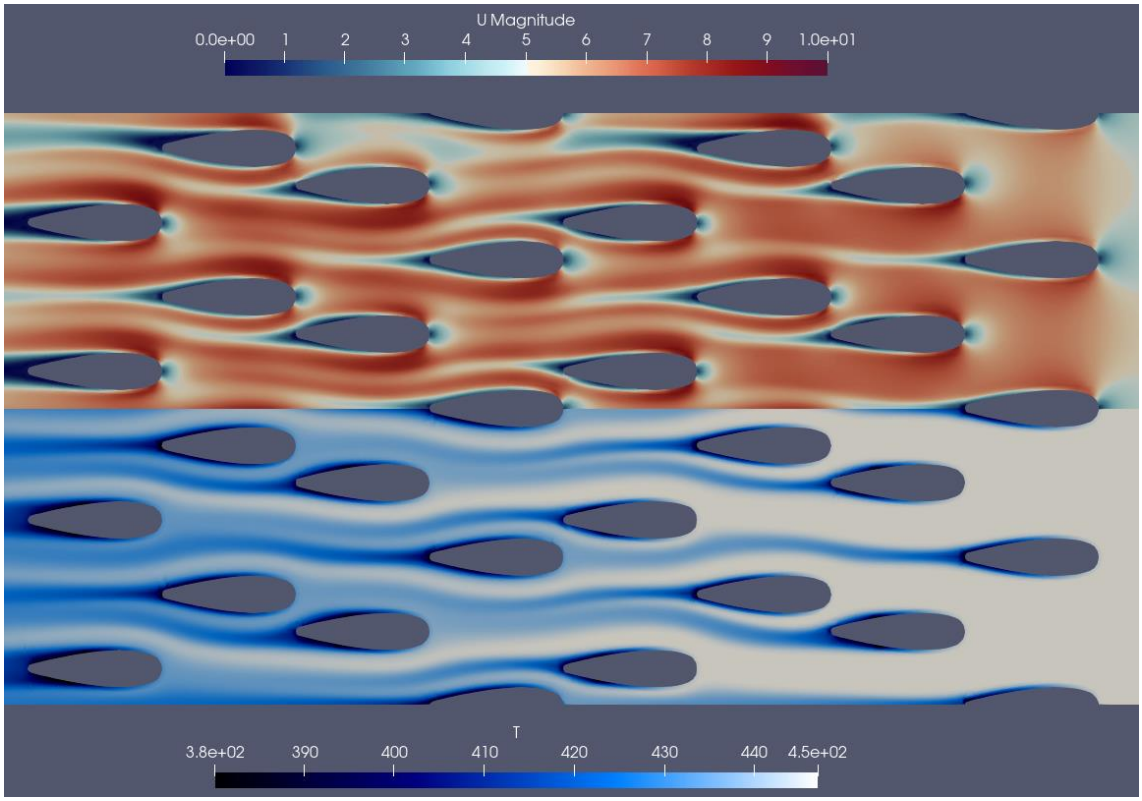

Figure 28. Alternative tube staggering to avoid array directionality.

The reason for area density loss in staggered arrays is the **interference of adjacent banks at low pitch.** For these geometries, at under 15mm lateral pitch, the gap between adjacent banks becomes so low that high flow separation occurs at the leading tube. This effect is well demonstrated in Figure 29. The separation causes increased pressure loss and reduces the effective heat transfer area, mitigating the benefits of tube staggering in the first place. The effect was demonstrated with all tested staggering configurations. This phenomenon could possibly be remedied by using a different tube geometry and/or using higher longitudinal pitch, but this shall remain the subject of future work.

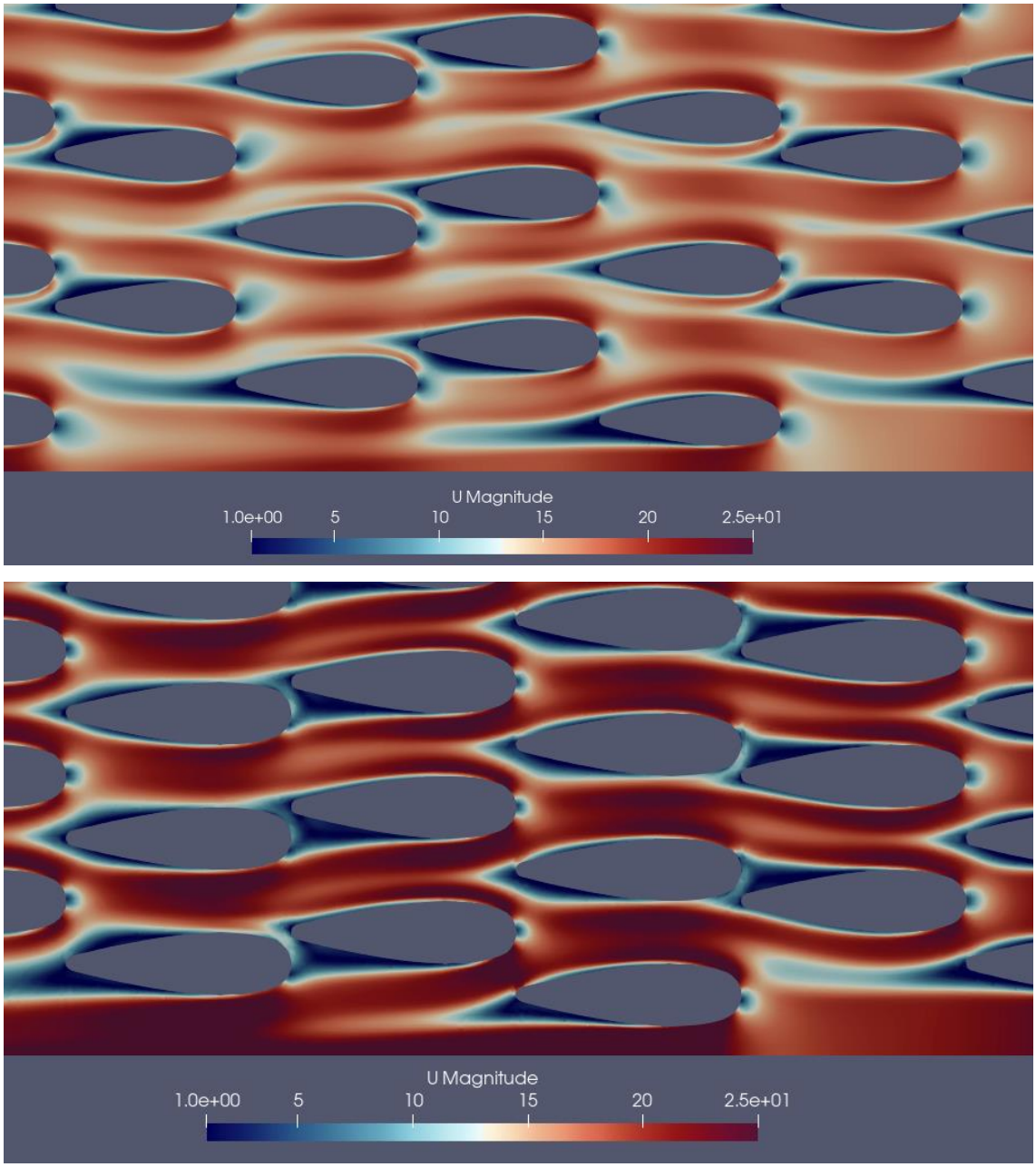

Figure 29. Closeup of the velocity field around staggered banks of tubes at 15mm (top) and 10mm lateral pitch.

3.2 Area density promoters

3.2.1 Secondary surfaces

Secondary surfaces are heat exchange surfaces, which are in direct contact with only one of the working fluids. A typical example of secondary surfaces are the fins in a tube-fin heat exchanger, commonly used in air-water HX: s. The main reason for using secondary surfaces is in applications where one of the working fluids has a significantly lower heat transfer coefficient. In these cases, the heat transfer surface area can be increased with

secondary surfaces to offset this imbalance, at the cost of extra material usage and friction losses on the finned side. (Kays & London 1984)

Secondary surfaces (fins from hereon) are challenging for additively manufactured heat exchangers for multiple reasons:

- Fins should have low thickness (<<1mm) for high efficiency
- Fins should be at an acute angle to the primary surface to reduce friction losses
- The intersection of primary and secondary surfaces can be structurally difficult
- Fins can have long distances of unsupported, thin structures that are difficult to fabricate in SLM methods

Perhaps the most difficult factor in designing AM secondary surfaces is the choice of build direction. All powder-bed manufacturing methods severely limit the possible orientation of a part being built. This is due to the requirement of supporting the surfaces being built. Any possible support structures are often removed after the part is built with cutting or machining. In this use case, support structure is extremely difficult due to the large size and cubical shape of the final precooler. Thus, the whole piece should be built in such a way to avoid any support structures in the core. Secondary surfaces represent another complication in the manufacturing process, as illustrated in Figure 30. Only the purple-coloured orientation requires no internal support structures, but even it requires supports on the outside. It is even possible to have support structures on the **inside of tubes** if they are shaped and oriented in a particularly difficult manner. Due to these difficulties, secondary surfaces are not considered attractive in this use case unless they are **required to reach the required power density**, which is their main purpose in any heat exchanger.

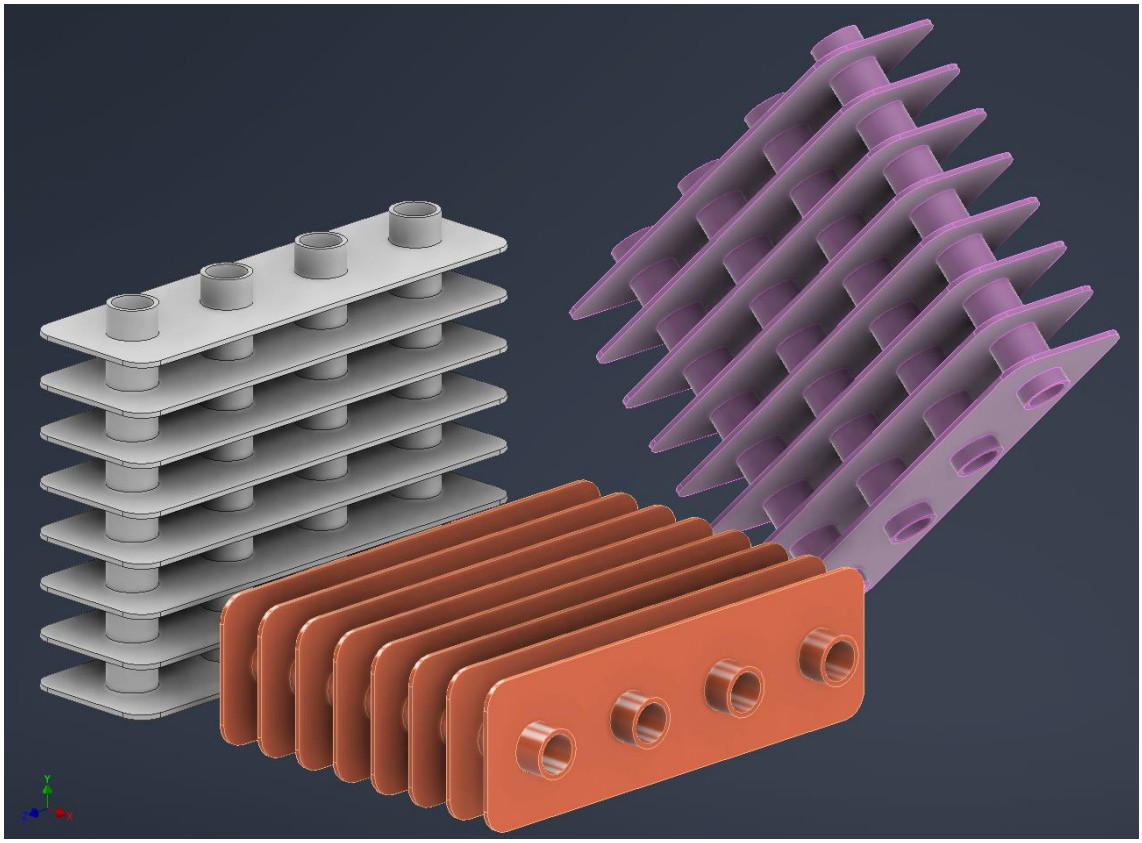

Figure 30. Some possible printing orientations of a simple fin-tube geometry.

Secondary surfaces were simulated in a similar setup to airfoil tubes, and their geometry is presented in Figure 31. The simulated geometry is an airfoil-tube array with 1.6mm thick fins connecting adjacent banks of tubes. This fin configuration increases mixing and keeps the maximum distance of solid material to coolant as short as possible. The pitch of these fins was then varied to see if they provide a substantial performance benefit.

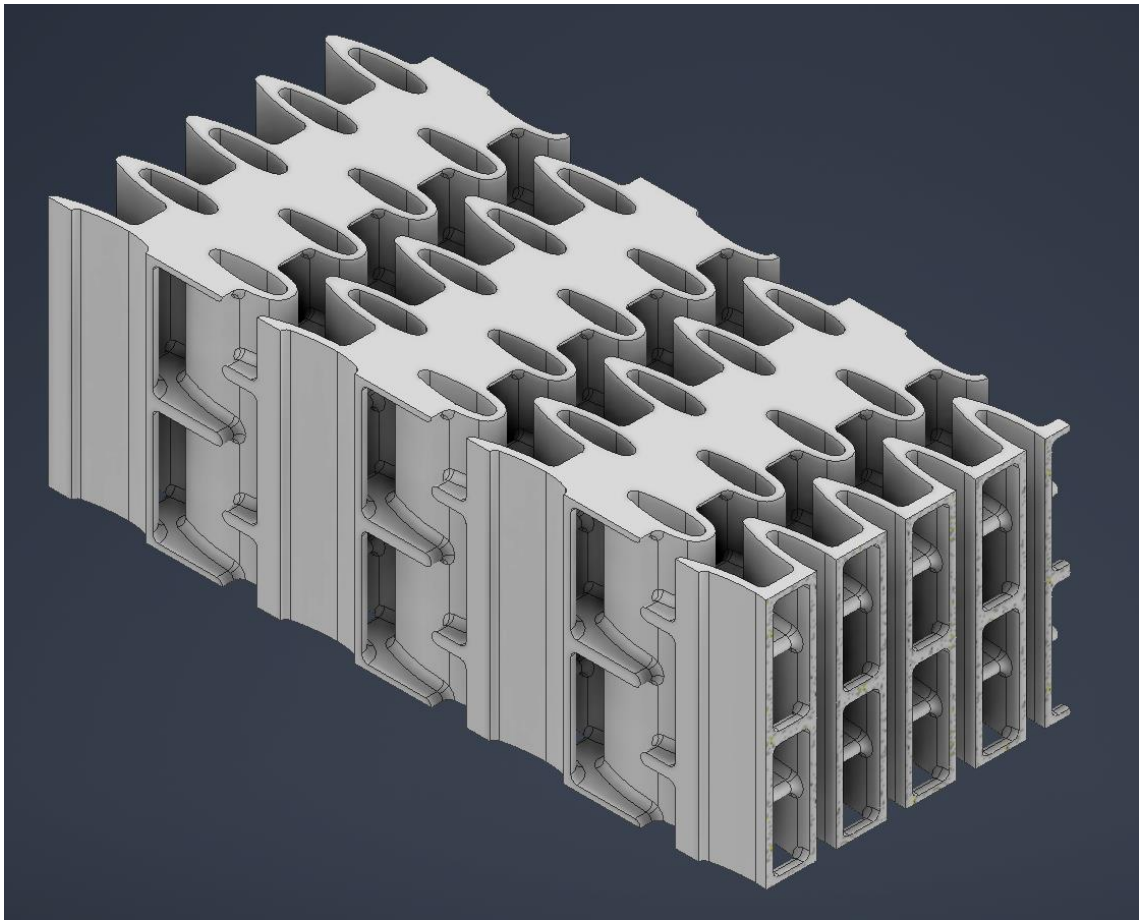

Figure 31. Section view of simulated fin-tube geometry.

As seen in Figures 32 and 33, the finned geometries perform as expected, the pitch in the charts refers to the separation of fins in their normal direction. Fin-tube geometries provide high power density at the cost of efficiency, with the behaviour trending towards the non-finned baseline airfoil performance. Unless another way to increase the power density is found, **secondary surfaces remain an option if their manufacturing challenges can be overcome.** This is especially true if more time and effort can be spent on finding a high-performance secondary surface geometry. Additive manufacturing grants high design freedom but this is useless unless a clear design path or geometrical target is found, and in the case of secondary surfaces, finding it has proven difficult as indicated by the multitude of different geometries found in the literature.

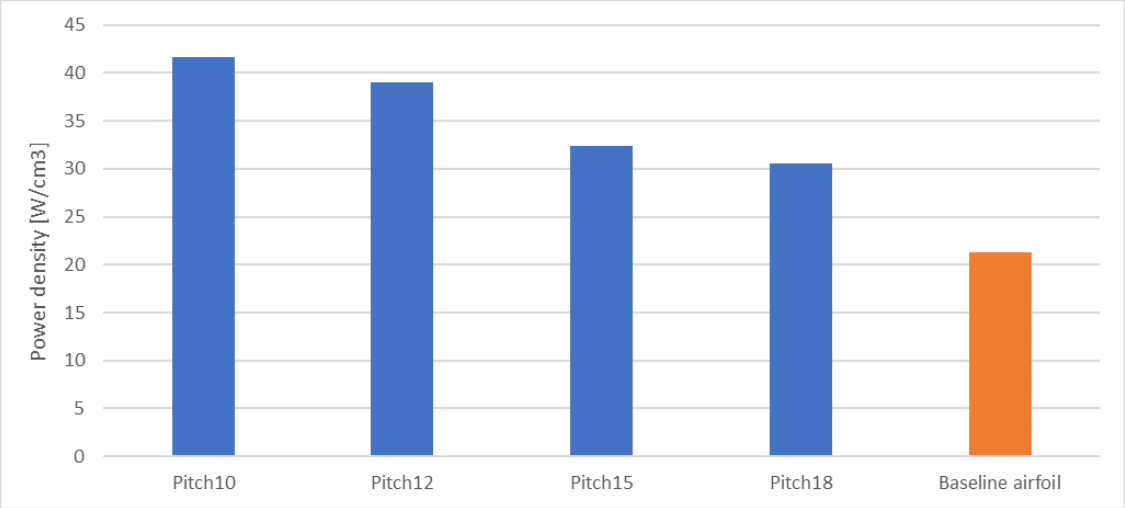

Figure 32. Power density of investigated fin-tube geometries.

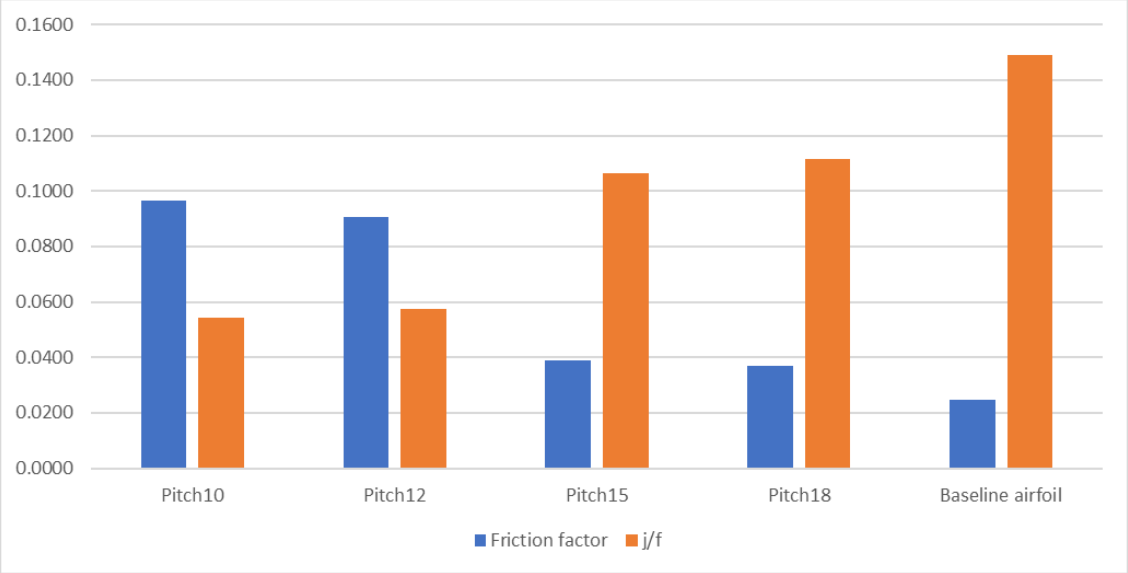

Figure 33. Performance characteristics of investigated fin-tube geometries.

3.2.2 Oval tube shape

Airfoil tubes can provide good friction characteristics but lack in area density when compared to typical round or flattened tube geometries, unless secondary surfaces are implemented. It was also postulated that the variance in free-flow area across the flow length could cause avoidable pressure losses due to repeated acceleration and deceleration of the flow. Thus, an oval shaped tube geometry adhering to the minimum dimensional constraints was created. This geometry, presented in Figure 34, was then studied by varying the lateral (blue) and longitudinal (red) pitch. The resulting area densities are presented in Figure 35 with reference Kays & London case in green, oval tube geometries in blue and airfoil tube geometries in orange. The resulting oval tube geometry is still

limited in surface area density, reaching only ~20% higher density at equal lateral pitch. Because the chord length is ~5mm shorter for the oval tubes, they can be stacked much tighter longitudinally, explaining the increase.

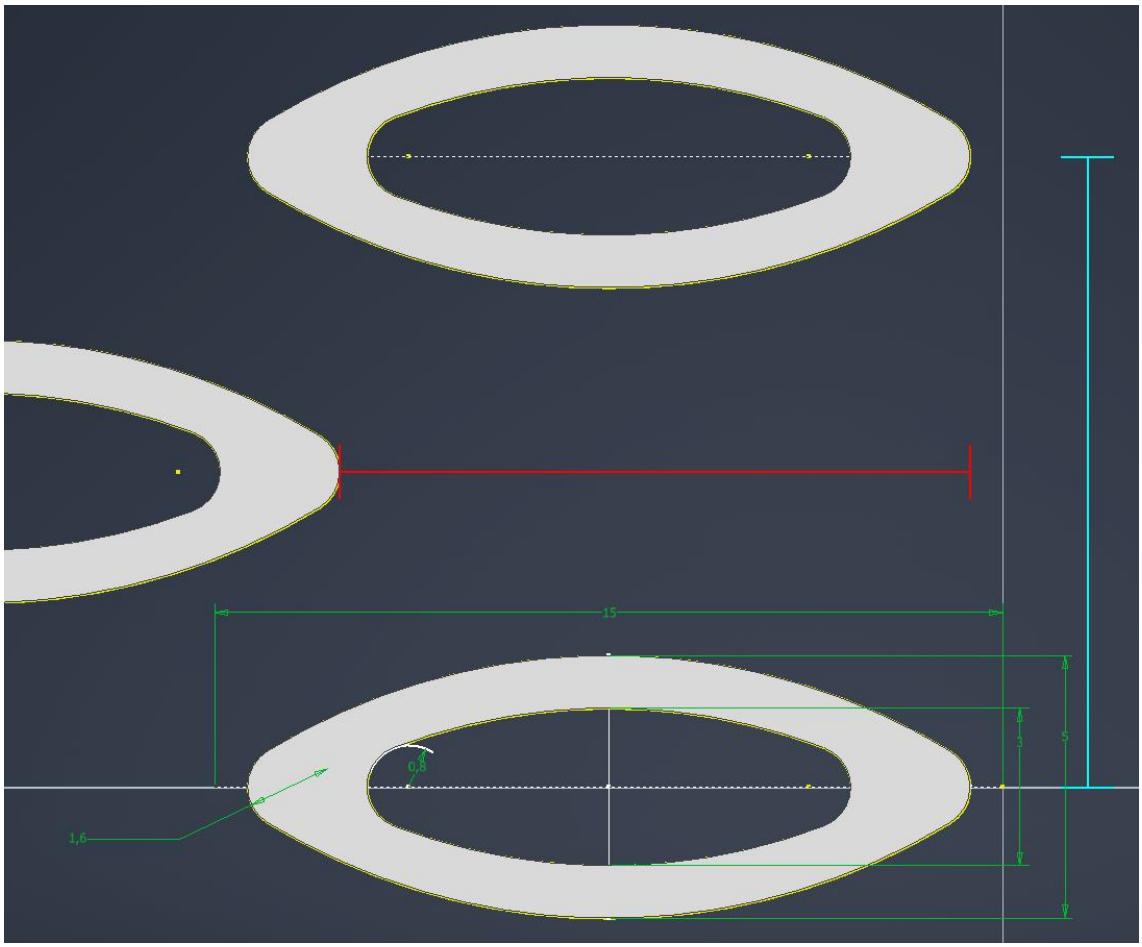

Figure 34. Minimum-sized oval tube geometry.

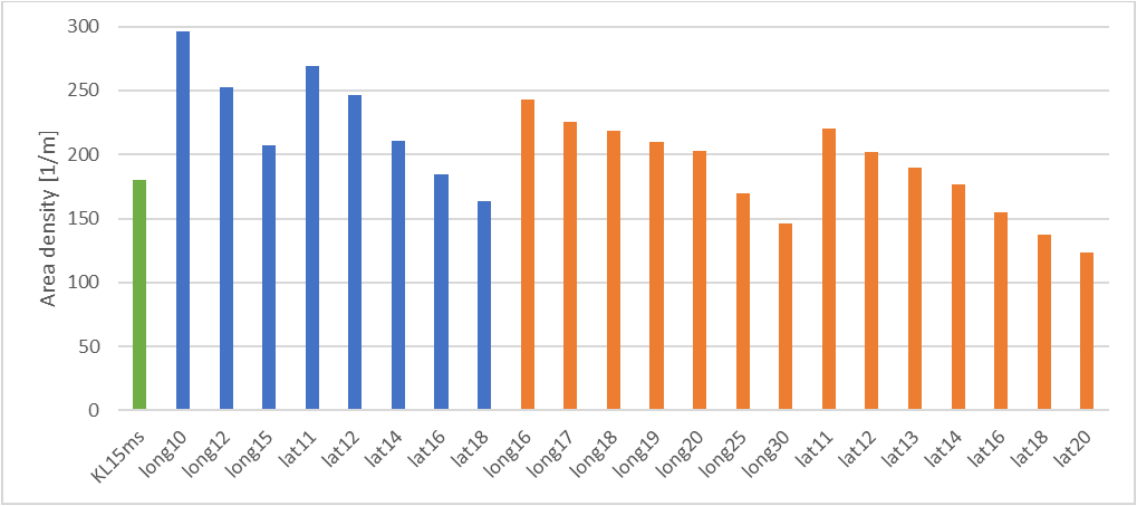

Figure 35. Area densities of investigated oval (blue) and airfoil (orange) tube geometries.

When simulated at the same conditions as airfoil tubes, oval-shaped tubes are inferior to airfoil shapes in friction but can overtake them in heat transfer coefficient and power density as seen in Figures 36 and 37. When compared to airfoil arrays, oval tubes exhibit similar dependency on longitudinal pitch but react more to variance in lateral separation. Peak performance seems to occur at longitudinal pitch of around the chord length of each tube, as was the case with airfoil geometries. Oval tube arrays do allow higher power densities than airfoil tubes due to the increase in surface area density, but also due to their geometry: oval tubes have less variance in flow velocity near their surface, at least when they are stacked closely enough. This is due to the more even distribution of free-flow area, as demonstrated in Figure 38. Even though the nominal free-flow area fraction is 0.5 for both airfoils and oval tubes, over the full length of a HX core the oval arrays vary in free-flow area much less than other geometries. Because the flow area remains closer to constant, so does the flow velocity in the channels between the tubes. It should be noted that the area density variance over a core length represents a design factor in itself, and the common way of only looking at the minimum free-flow area might not be good enough with more complex HX core geometries.

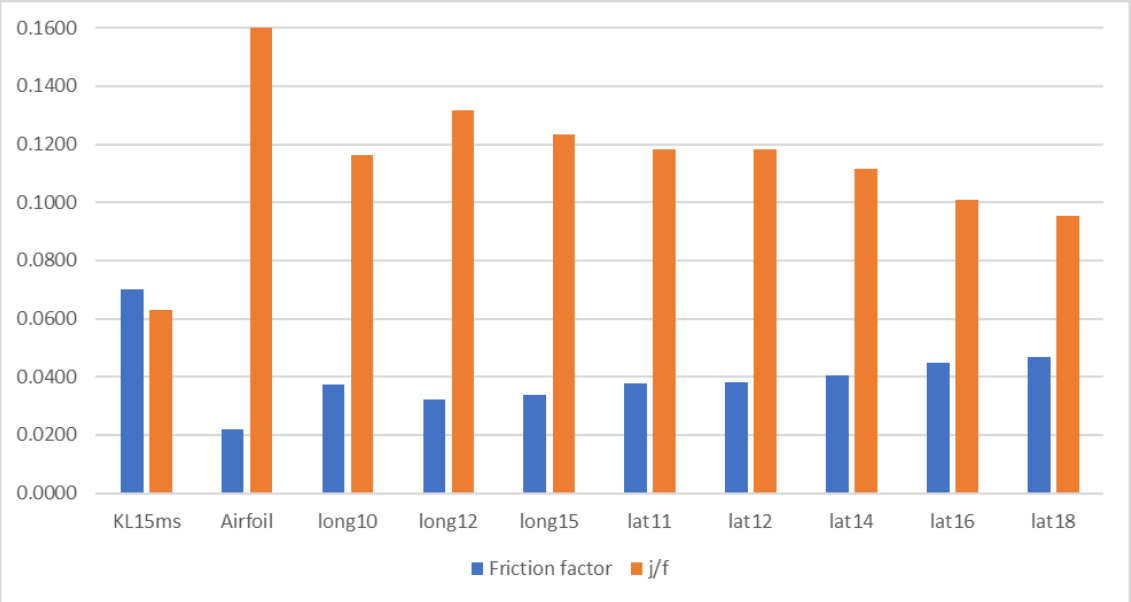

Figure 36. Performance characteristics of oval tube arrays.

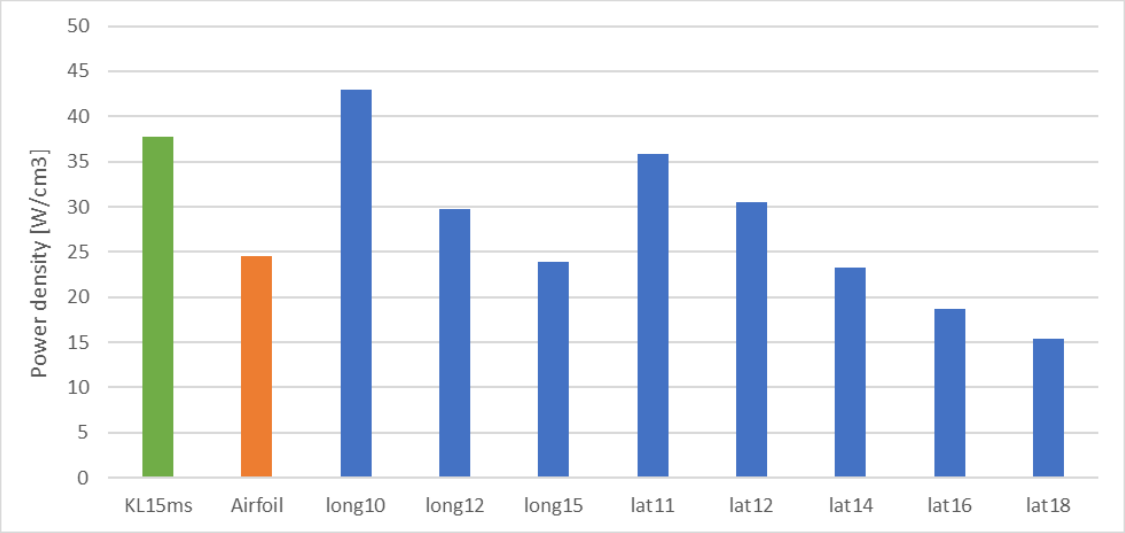

Figure 37. Power densities of oval tube arrays.

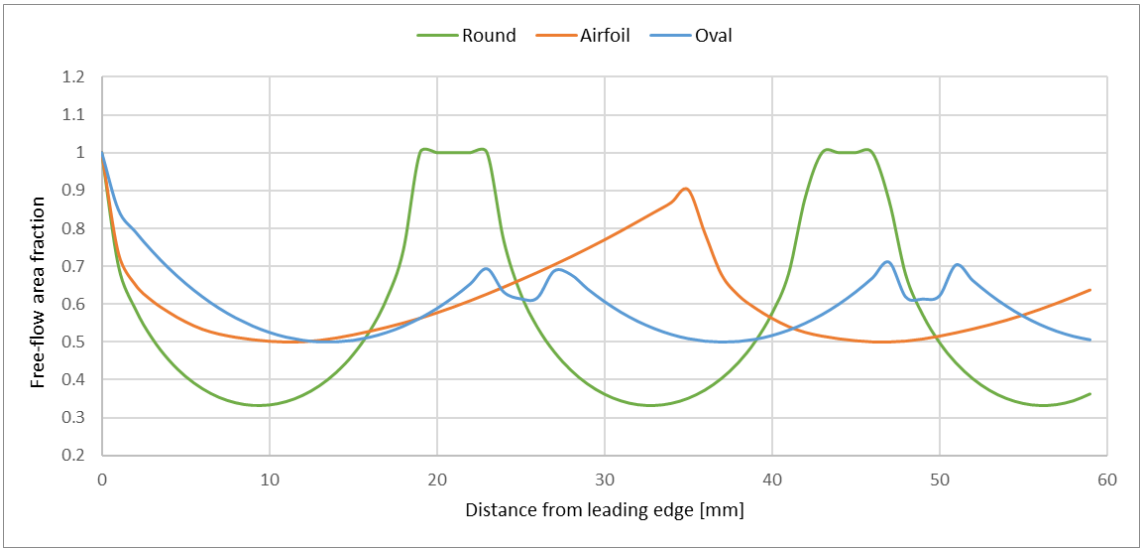

Figure 38. Free-flow area variation in flow-wise direction for Kays & London reference case ("Round"), airfoil tubes at 18mm longitudinal pitch and oval tubes at 12mm longitudinal pitch.

The more even velocity distribution of oval tube arrays is apparent in Figure 39. The next row of tubes forces the flow to closely follow the trailing edge of the previous row, resulting in thin boundary layers and less stagnation at the leading edge of each tube. This contrasts with airfoil geometries which exhibit thicker boundary layers at their trailing edges and flow separation at high longitudinal pitch. Higher flow velocities near tube surface leads to higher heat transfer coefficients but also higher surface friction. This is most likely the main reason for the increased power density and friction loss of oval tube geometries when compared to airfoil tubes.

Oval tubes are however not immune to flow separation. If the separation between tubes is too high in either direction, flow will separate early as demonstrated in Figure 40 for lateral and 41 for longitudinal pitch. Too high lateral separation is especially detrimental for HX performance as only a small section of the tube is in contact with high velocity airflow. Moreover, the "shadow" of cooled air from the previous row of tubes forms most of the boundary layer of the next row, reducing the effective temperature difference. The width and thus effect of this shadow is directly related to the point of flow separation of each row. This finding is in harmony with results from airfoil geometries, where flow separation also had a detrimental effect on heat exchange performance. Oval tube geometries represent a high-power density alternative for airfoil shapes. They become more attractive at high allowable pressure loss and can be considered an intermediate step between round and airfoil tube arrays. For the use case at hand, **airfoil tubes remain the preferred option due to their superior friction characteristics.**

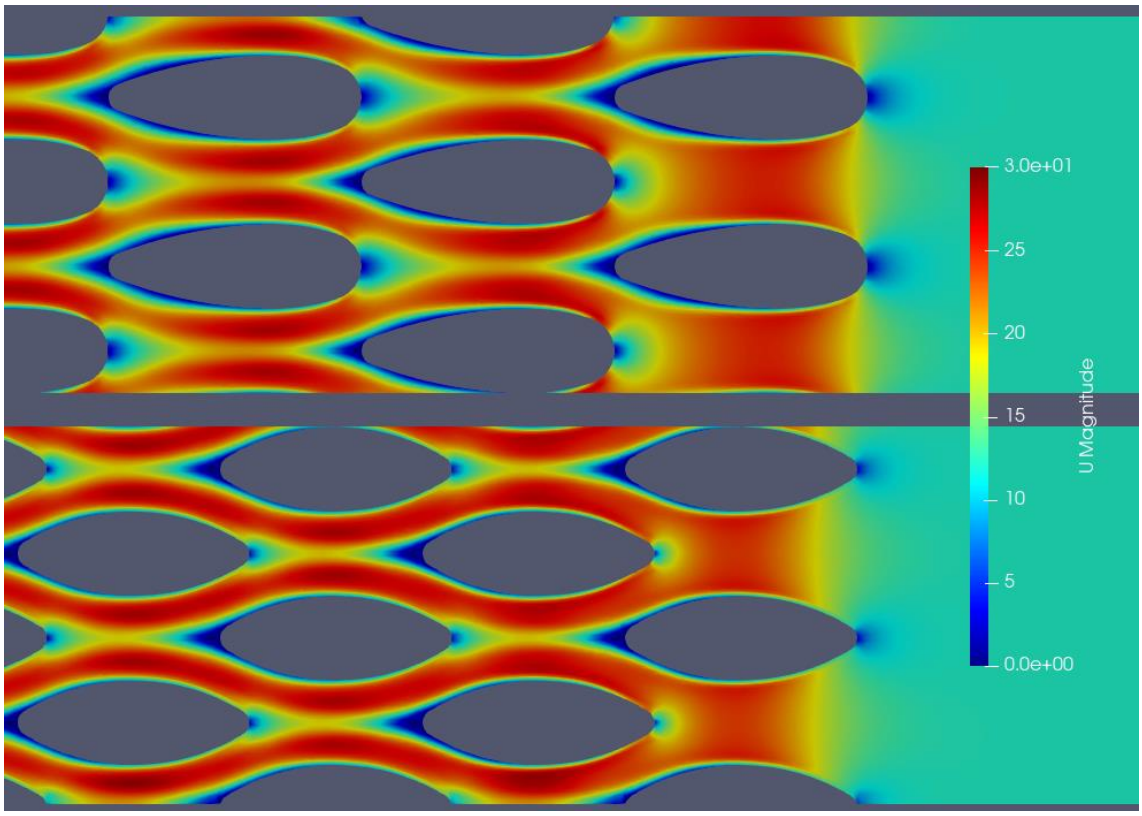

Figure 39. Closeup comparison between airfoil and oval tube velocity distribution.

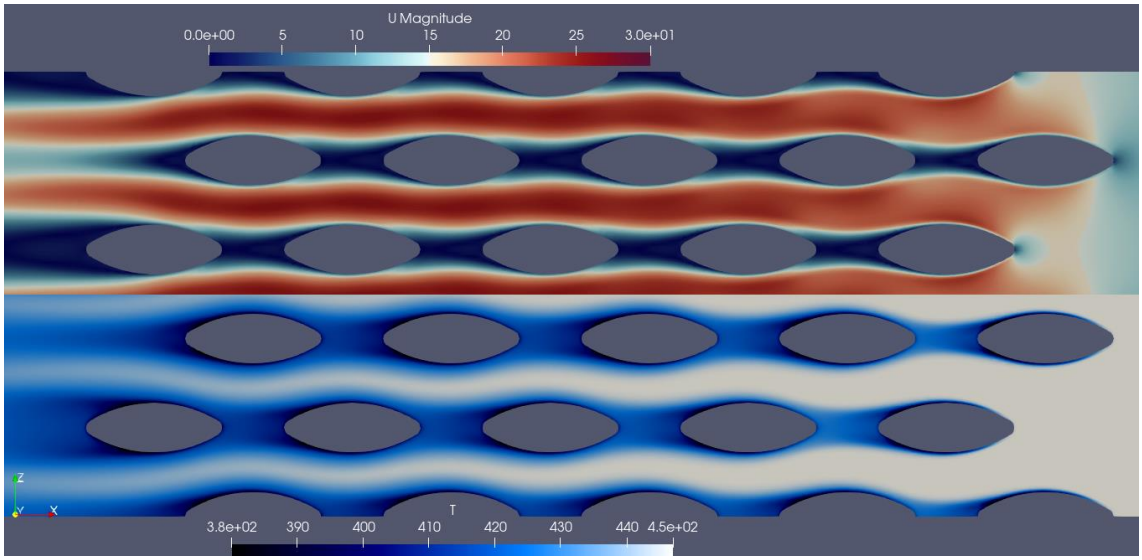

Figure 40. Oval tube at high (15mm) lateral pitch with velocity (black-blue-red) and temperature (black-blue-white) fields visualized.

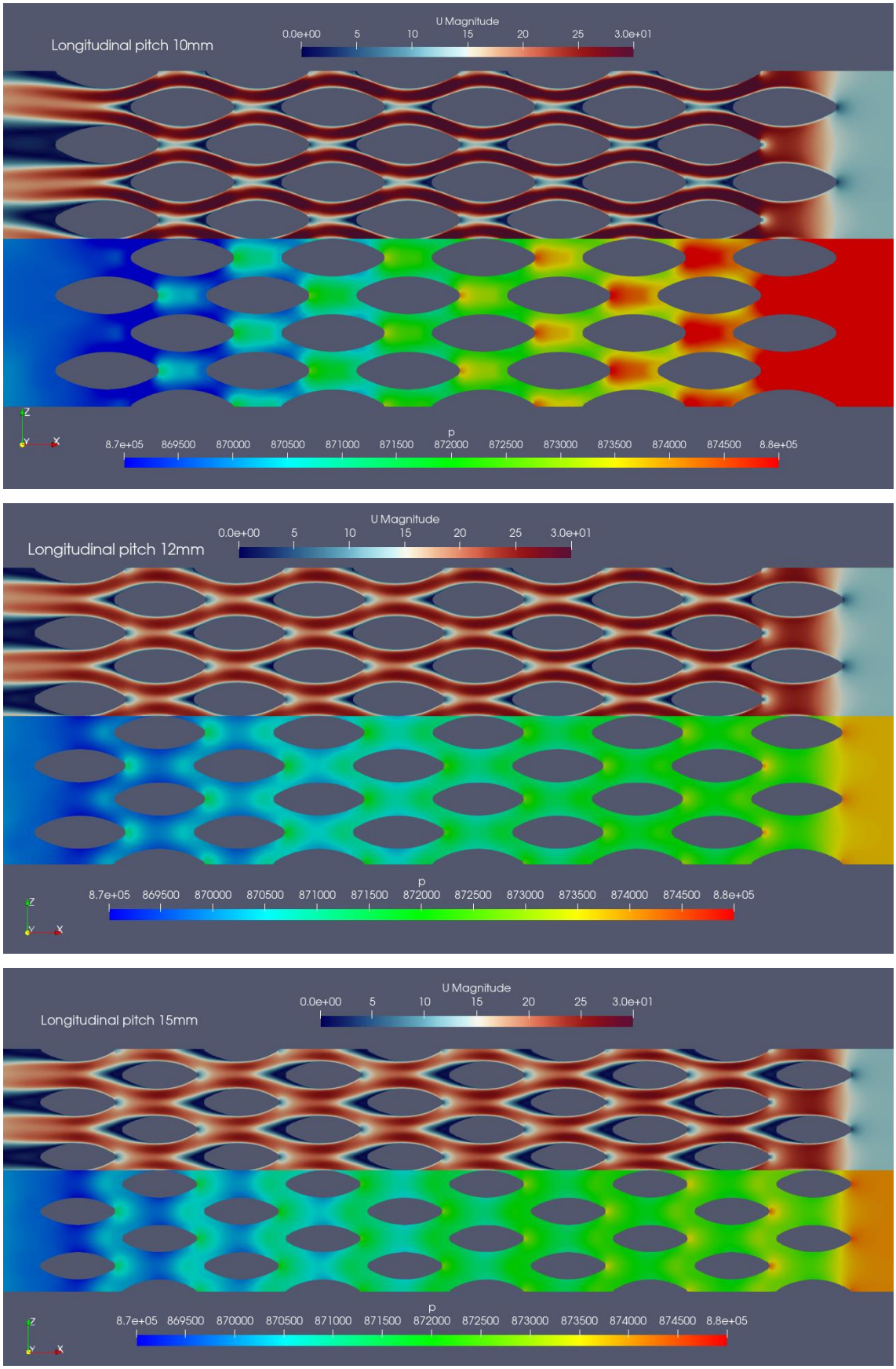

Figure 41. Velocity (black-blue-red) and pressure (blue-green-red) fields of oval tube arrays at varying longitudinal pitch.

3.3 Core entry and exit treatment

3.3.1 Pressure loss mitigation

As stated by Kays & London (1984, p. 35-49), pressure losses in a HX core are not only caused by the friction with the heat exchange surfaces, but also due to the effects of flow entering and exiting the core. Typically, these losses are accounted for by the overall friction factor or by using a separate empirical coefficient. For consistency in this work, all losses in a HX core are included in the friction factor. The entry and exit losses can still be studied and an attempt to mitigate some losses was made. These efforts were simulated with an oval tube geometry at 12mm longitudinal pitch to facilitate comparisons when no entry or exit treatment is implemented.

For core entry, 2 cases were studied: one with the first bank of oval tubes replaced with an airfoil shape of similar chord and thickness, as seen in Figure 42, and a case with the 2 first banks replaced with airfoils. The reasoning behind this approach is to try and combine the best characteristics of both oval and airfoil tubes: the high power density and low friction respectively. It was postulated that airfoils should yield most benefit before the flow is shaped by the tube array, and oval tubes can then provide the desired power density. Core exit losses were studied with 2 geometries: a case with the last bank of oval tubes split at their half distance, as seen in Figure 42, and one with the last bank of tubes replaced with "boat-tail" oval tubes shown in Figure 44. These shapes were chosen to give the exiting airflow a distinct point of separation: both oval and airfoil tubes exhibit flow separation at the trailing edge of the last bank, but the point where this happens is not consistent as was demonstrated earlier.

It should be mentioned that these designs represent but a fraction of the possible design space. A major factor behind these choices is the desire to stay within the geometric constraints described in section 3.1. Minimum wall and water channel thickness bounds prohibit the design of many interesting geometries, for example a smooth transition between thin and thick tubes to control the free-flow area. While tubes without a water channel are possible, they are not without issues. They don't offer much heat transfer potential and can be structurally challenging due to thermal stresses in operating condition transients. Similarly, lower wall thicknesses or feature sizes are considered impossible with the chosen manufacturing method due to lack of prototyping.

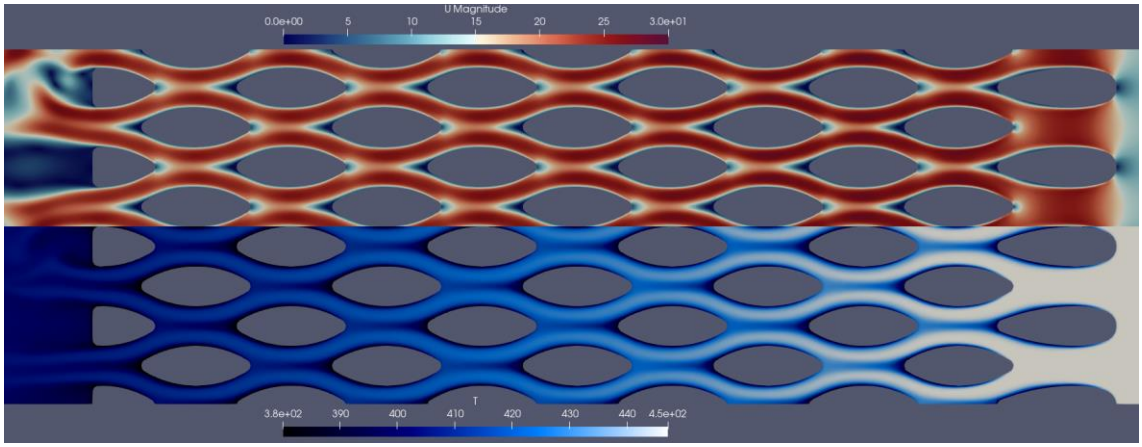

Figure 42. Entry/exit treatment simulation with a leading airfoil tube and split-oval trailing tube banks, with velocity (black-blue-red) and temperature (black-blue-white) fields visualized.

Numerical results of these simulations are shown in Figure 43. While a split oval exit treatment offers no real benefit over the baseline, both the leading airfoil bank and boat-tail exit cases show a slight improvement in heat transfer without a corresponding increase in friction. The reason for the good performance of a boat-tail trailing tube bank is apparent in Figure 44: unlike in full oval-tube geometries, the last bank is contacting high-speed airflow with the most of its surface area. The formation of a von Kármán vortex street is also apparent behind the last bank. This can indicate good flow mixing and a fast transition to smooth and uniform flow after the core. It can be said that at least a boat-tailed final bank can be implemented in oval or airfoil tube arrays without high risk of performance degradation.

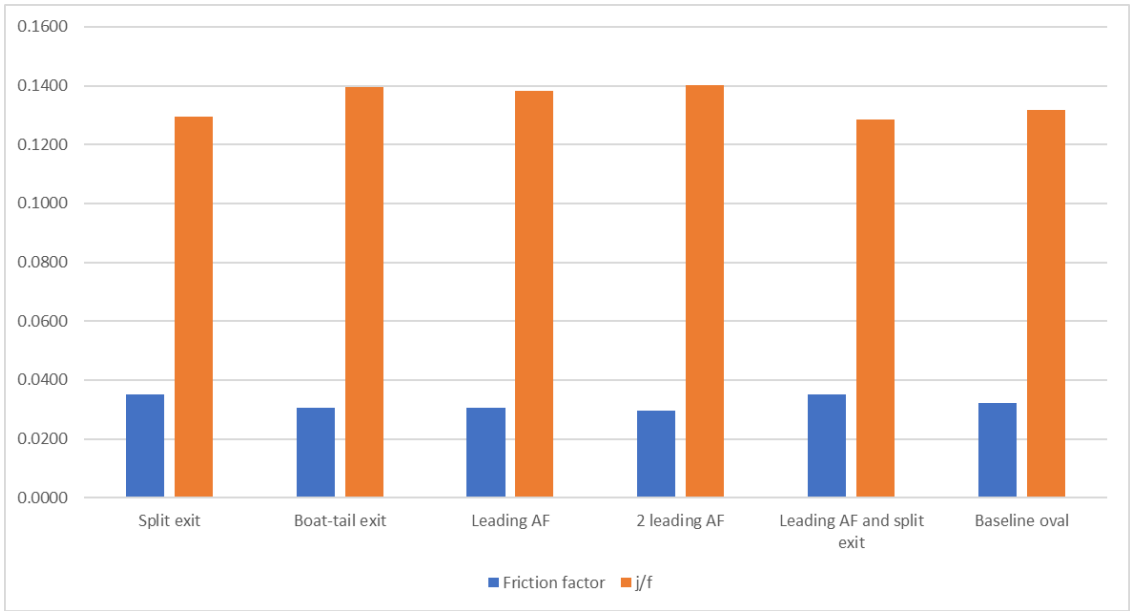

Figure 43. Numerical results of entry/exit treatment simulations.

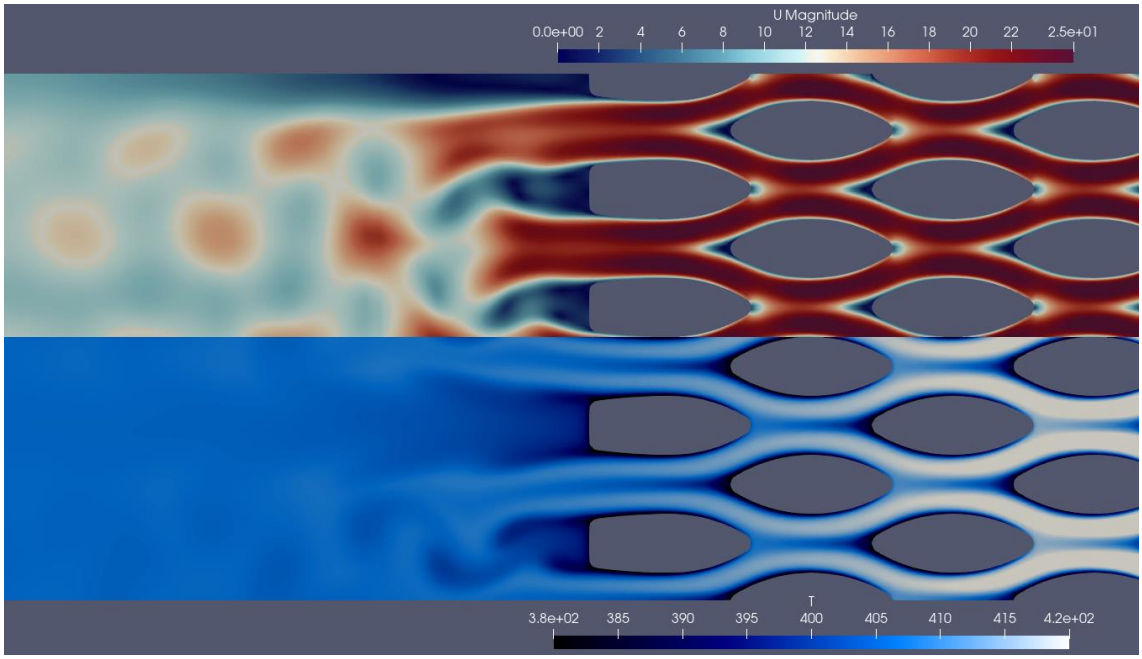

Figure 44. Detail of a simulation with boat-tail final bank with velocity and temperature fields visualized.

3.3.2 In- and outflow uniformity

While core entry losses are important mainly for the pressure loss, core exit geometry is important for another reason: **outflow uniformity**. Because the cooler designed here is part of a system, the precooler outflow uniformity can influence the existing charge air cooler further downstream. Outflow uniformity was analysed using an existing OpenFOAM-postprocessing function. Outflow uniformity of different geometries at 30mm behind the array is presented in Figure 45. A value of 1 represents fully smooth and uniform flow in this chart. It should be noted that due to transient effects like trailing edge vortex shedding, these numbers are a time-averaged value and vary up to ±0.05. Furthermore, the actual outflow uniformity is also dependent on the shape of the duct where this geometry is placed. To remove a simulation variable, they were tested here without a physical exterior duct, but this effect should be kept in mind when designing a full-scale heat exchanger core. The results achieved reinforce the positive attributes of airfoil geometries and boat-tail exit treatment, as they do not compromise the outflow uniformity. Round tubes and split-tube exit treatments perform poorly, as expected from the qualitative results.

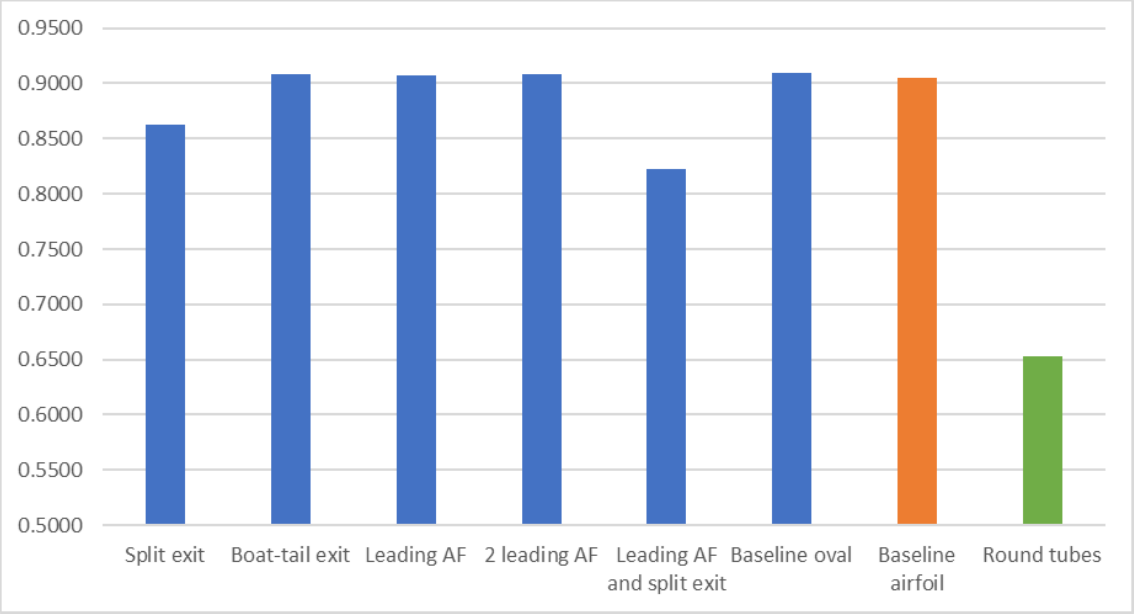

Figure 45. Outflow uniformity of various heat exchange geometries.

The effect of inflow uniformity on heat exchanger core performance is vastly more difficult to evaluate. This is mainly because the **flow conditions right after the turbo-compressor are not known** and are difficult to estimate. This is a problem not only for the precooler design but also for the design of the piping leading to the precooler, both for pressure loss mitigation and flow uniformity. Because the physical space for inlet piping is limited, and the turbocharger and charge air cooler positions are fixed, a set of possible precooler position configurations was drawn and simulated. The main concepts are presented in Figure 46, with the compressor outlet in green, precooler in red and charge air cooler in cyan. All intake piping in white is considered possible to change and to reduce costs and effort the piping downstream of the CAC (blue) is considered final. Because the funnel leading to the CAC must be redesigned to accommodate the precooler, an effort was made by colleague Simone Dorbolo to design an optimized, smoothly expanding shape for it and the required intake piping to house the added precooler. These concepts were then simulated and analysed for flow losses and charge air cooler intake uniformity. The simulations were run both with a straight-flow inlet and a swirling-flow inlet with 30% swirl in the intake flow to accommodate the unknown compressor outlet conditions.

Of the tested configurations, one with precooler integrated to the funnel was chosen (top-left in Figure 46). This geometry performed second-best for flow losses and was the best for CAC intake uniformity and requires only a single piece of new piping to be manufactured compared to 2 or more for the other configurations. The simulations can be

considered preliminary, as both the CAC and precooler were represented by a *porous zone* with approximated pressure loss and heat exchange in place of their actual 3D-geometries. This was done to reduce the required mesh cell count by several orders of magnitude, as the small features in the coolers require a huge number of cells to represent accurately.

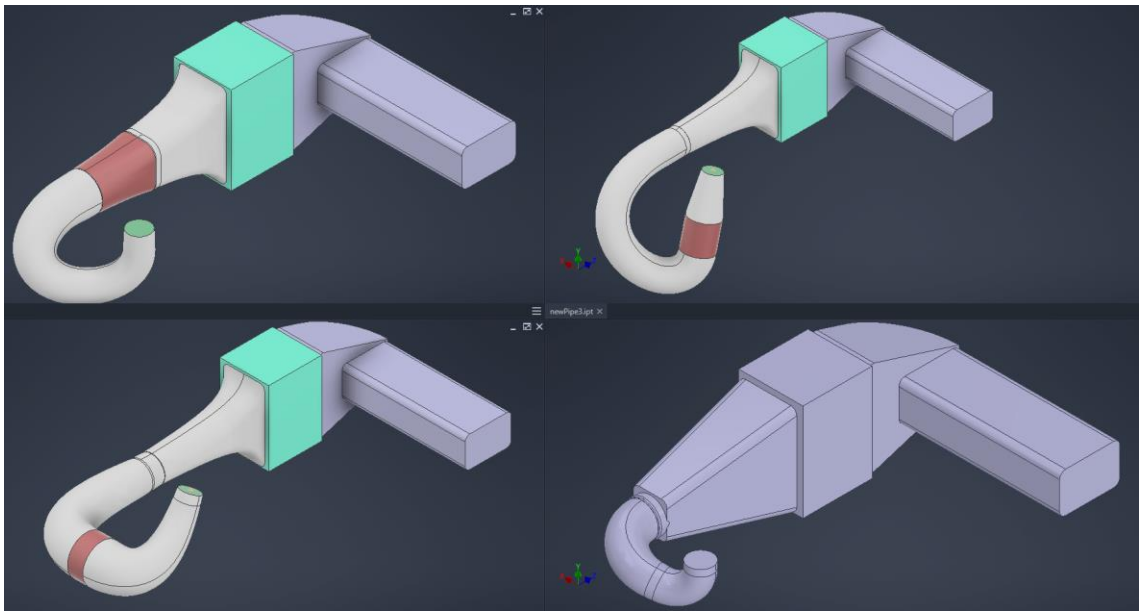

Figure 46. 3 possible intake pipe configurations with added precooler, and the existing setup at bottom right.

As seen in Figure 47, the sharp corners of the existing intake funnel cause high flow separation which results in ununiform flow into the CAC. The change to a smooth funnel and the addition of a precooler to even the intake swirl vastly improves the situation, with **CAC intake uniformity index jumping from 0.55 to 0.9**. This should increase the performance of the existing charge air cooler with no additional cost, as the pressure losses are roughly equal between the two systems before adding precooler losses.

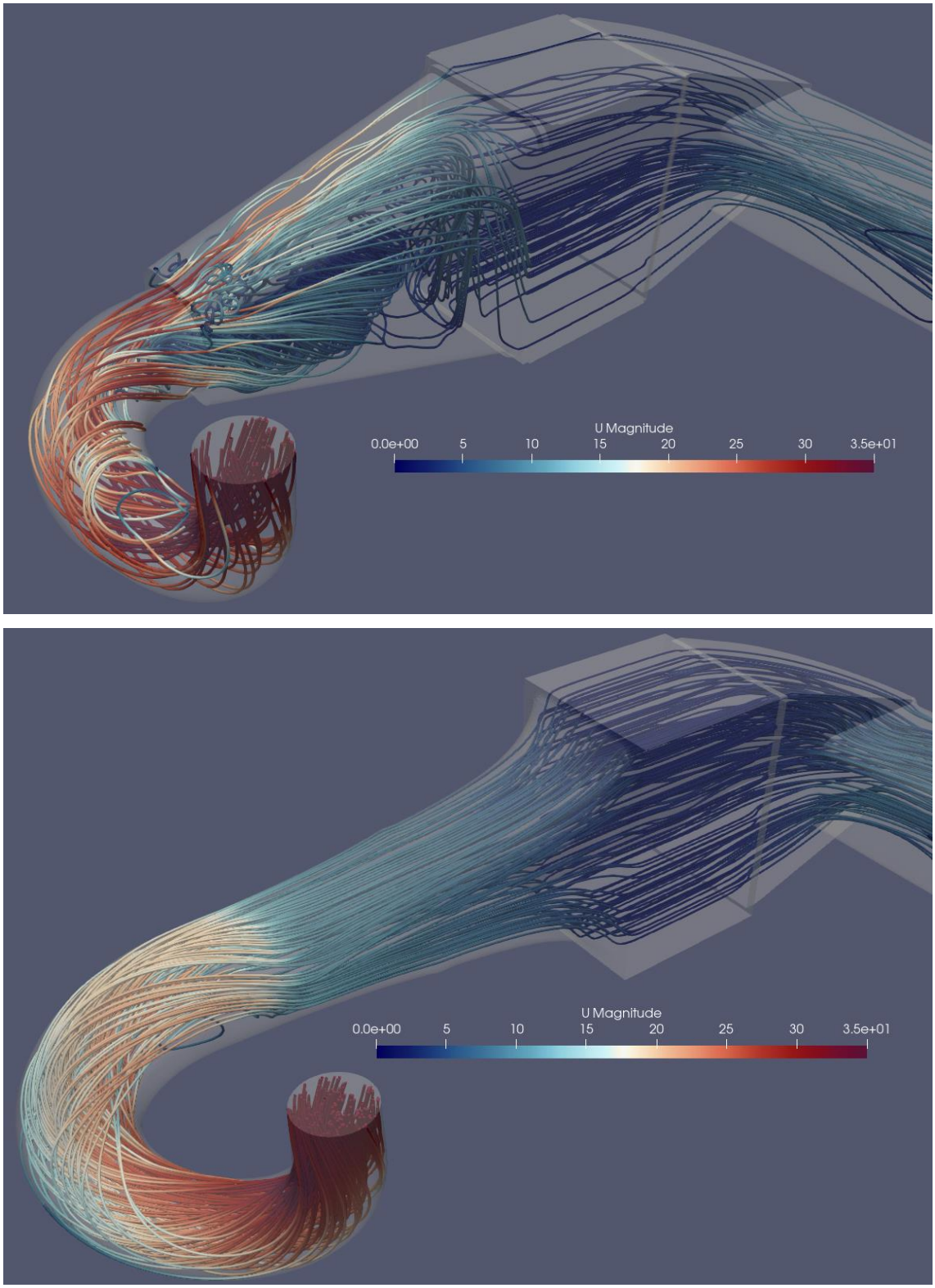

Figure 47. Velocity flow-field comparison of existing (top) and chosen intake configuration with streamline visualisation.

To test the intake pipe configuration with a fully modelled precooler, a scaled-down model of the intake pipe and precooler was created. This was done to reduce the required mesh cell count from ~50 million to 3.5 million, making the simulations feasible in a

reasonable time. Intake flow velocity was also adjusted to keep the core intake velocity at the expected value of 12 m/s. While this method is not perfect, it does allow the comparison between possible precooler core geometries in a more representative environment. Furthermore, the effects of a full scale precooler should more or less match the results found in the scale model due to similar Reynolds number. Still, to reduce the effect of downscaling on core performance, the piping downstream of the precooler was replaced with a straight pipe. The results from this scaled down model were complemented with simulations with just a straight pipe with the precooler inside, shown in Figure 48. Both cases were run with a straight inlet and inlet with 30% swirl. The results from these simulations are not directly comparable to the results presented earlier due to the different solver and geometry used, but the trends found should still apply.

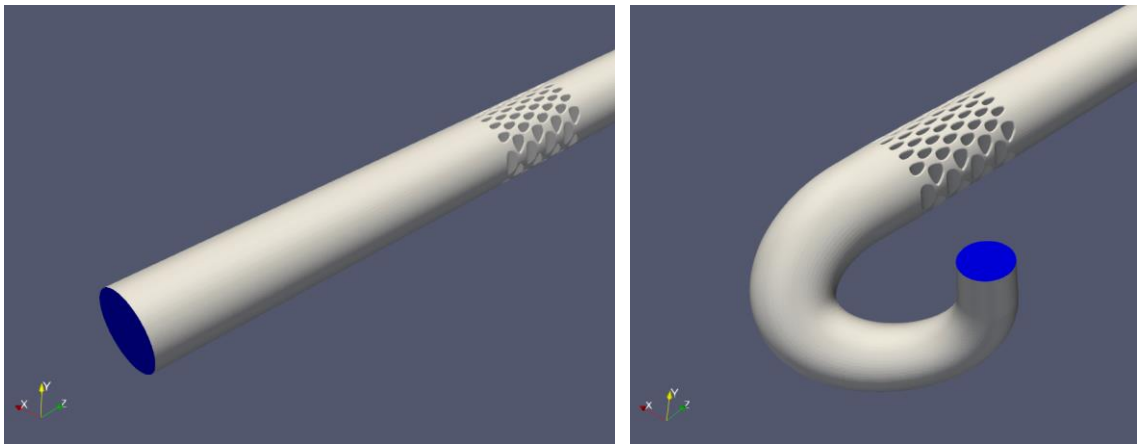

Figure 48. Scaled-down simulation models of intake flow variations with the inlet in blue.

The results from these simulations are presented in Figure 49 . Cases with “iP_” have the curving inlet pipe modeled, and “straight_” cases have the straight inlet. All of the cases provide good outflow uniformity with or without swirl in the inlet. Inducing swirl to the inlet flow seems to only increase the uniformity downstream of the precooler, which is to be expected as more flow is forced to the outside walls. The outside walls present a source of friction, causing the flow to tend to focus on the central section where the resistance is at its lowest. It can be assumed that increasing the inlet swirl increases the outflow uniformity, but it is hard to take this factor into account due to the unknown inlet conditions in the actual intake system.

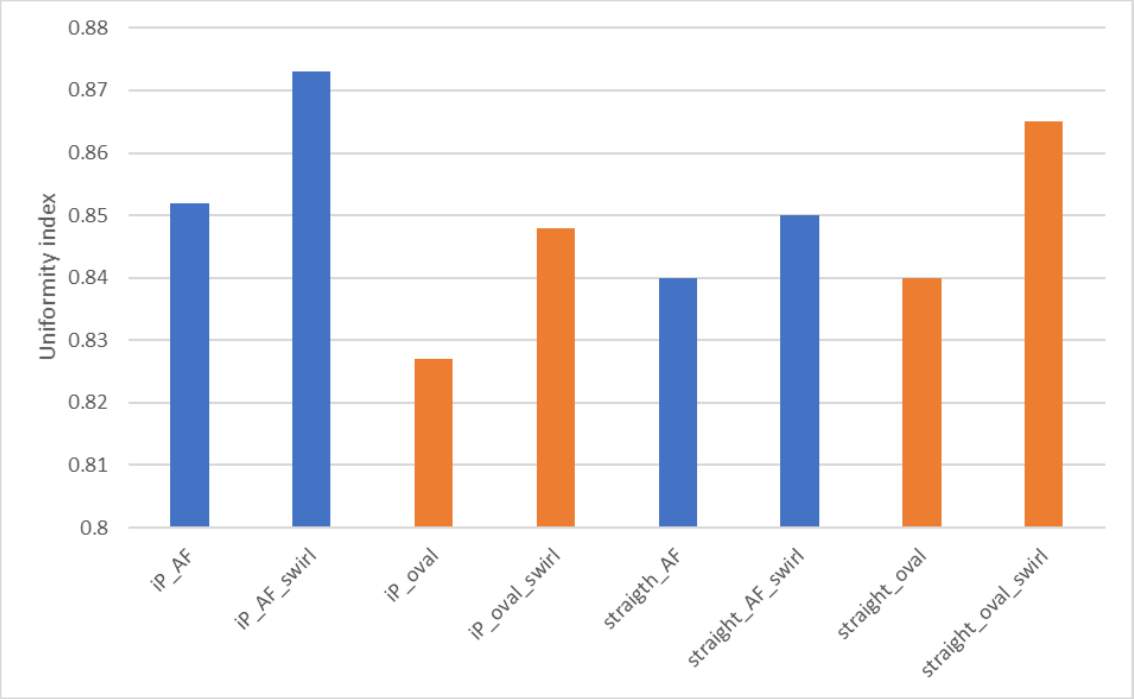

Figure 49. Outflow uniformity index of studied scale-model cases.

While inducing swirl in the inlet flow had negligible effect on overall pressure loss of the system, the curved intake pipe increased the loss by ~3500 Pa in all cases when compared to a straight inlet pipe. This is to be expected, as the curving and expanding pipe also requires a higher intake velocity for a given mass flow. Any intake pipe however represents another design problem: flow separation before the cooler array. This phenomenon can be seen in Figure 50, which is from the case iP_AF. Interestingly, neither the change to a curved intake pipe or a swirling inlet does not seem to affect the heat transfer rate more than 10%, with the **swirling and curved intakes performing the best**. This could be explained by the increased mixing provided by the uneven intake conditions.

All tested geometries seem to perform very well in the tested intake conditions. This is most likely due to the 50% flow area reduction caused by the precooler array. The flow is forced to stagnate and even out across the whole array, as the local static pressure increases rapidly when approaching the array. **Further work is required in optimizing the array and intake piping to match each other**, as there could be some performance gains to be had especially if the intake flow conditions are known better.

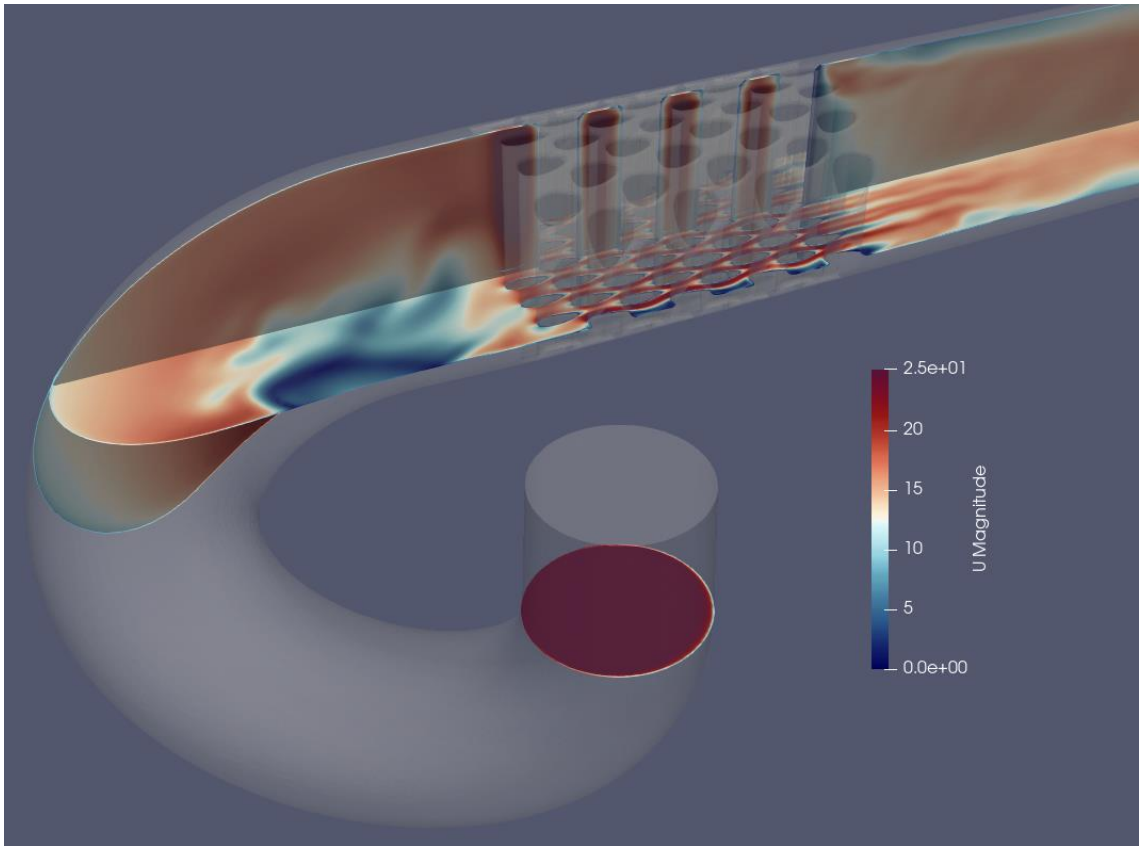

Figure 50. Snapshot of case "iP_AF" with velocity field visualized in two perpendicular cross sections.

3.4 Performance estimations

Concurrent with the simulation work presented here, design work on the mechanical aspects of the precooler was conducted by Simone Dorbolo at Wärtsilä. This work was kept mostly separate from the cooler core design to distribute the workload. The result of this work is the new intake system for the W6L20CR-DF laboratory engine, presented in Figure 51. As the inlet area and volume of the precooler core was placed as a priority, the precooler support structure was separated from the additively manufactured section. This meant that the final precooler size and shape of the precooler was different from the initial design goals presented in section 2.7. The final geometric properties and required performance parameters are presented in table 5. Especially important is the change from round to square cross section for the precooler core. This change causes **additional uncertainty for performance predictions due to the worse than expected inflow conditions**. While there certainly is room for optimization in the final design, this work can be considered out of scope for this thesis. For now, extra margins of error were added to the final performance estimations to account for this probable performance loss.

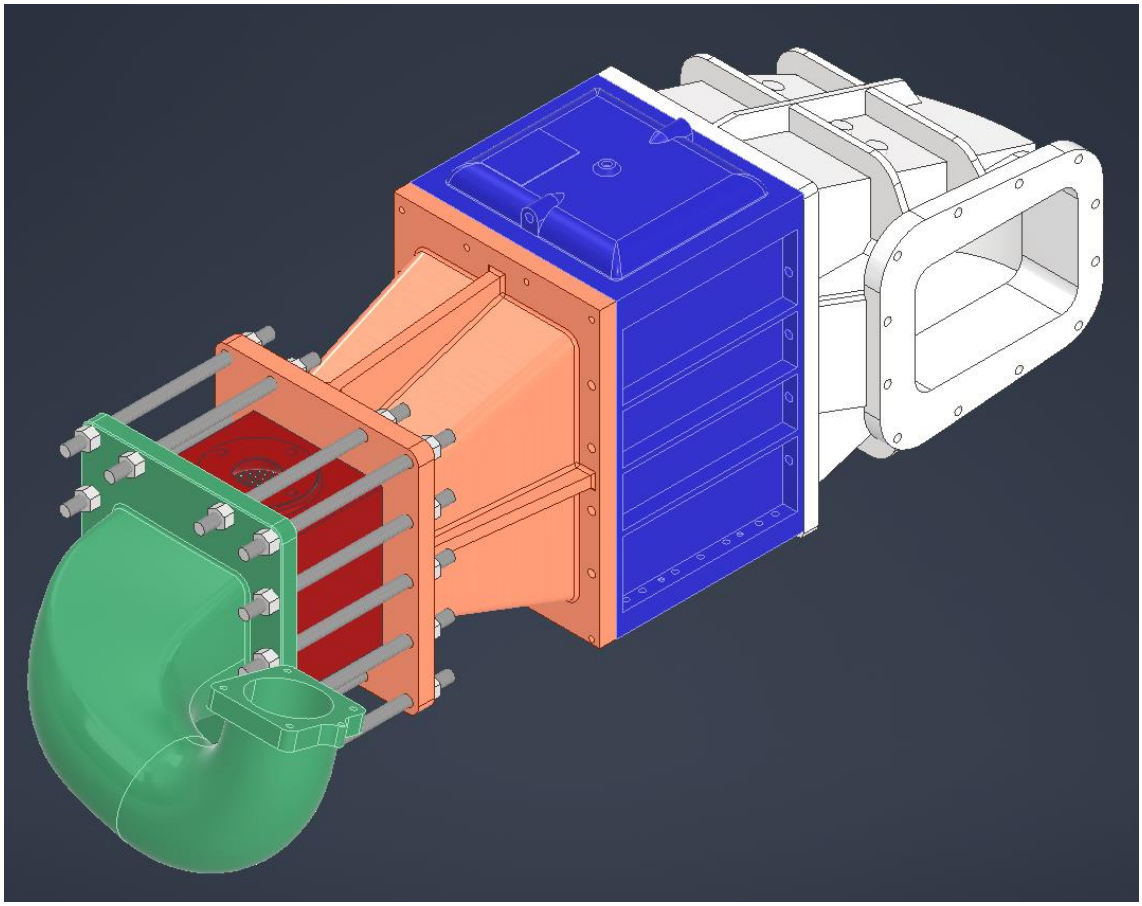

Figure 51. The final intake system configuration with added precooler in red, structural fasteners in gray, new intake pipe in green, new funnel in orange, existing charge cooler in blue and existing intake air receiver in white.

Table 5. Final precooler performance targets.

Inlet area	408 cm^2
Inlet velocity	8.9 m/s
Mass flow velocity G	120.5 kgm^2/s
Heat exchanger overall volume	898 cm^3
Overall heat exchange area A	2.18 m^2
Resultant Reynolds number Re	~47 000
Target heat transfer rate	160 kW
Target pressure loss	4000 Pa
Required heat transfer coefficient U	600 W/m^2K
Required power density	17.8 W/cm^3
Required friction factor f	0.0355
Required Colburn factor j	0.0039
Required j/f	0.1100

The added inlet area provided by the rectangular cross section, presented in Figure 52, **theoretically reduces the demands from the heat exchange geometry**. However, as flow through a rectangular section is never uniform, and even less so right after a turbo-compressor and a curving pipe, the performance targets were changed from **140 to 160 kW of heat transfer and from 5 to 4 kPa of pressure loss** to account for the high performance uncertainty. A final, full size heat exchange array was then designed to meet these performance targets.

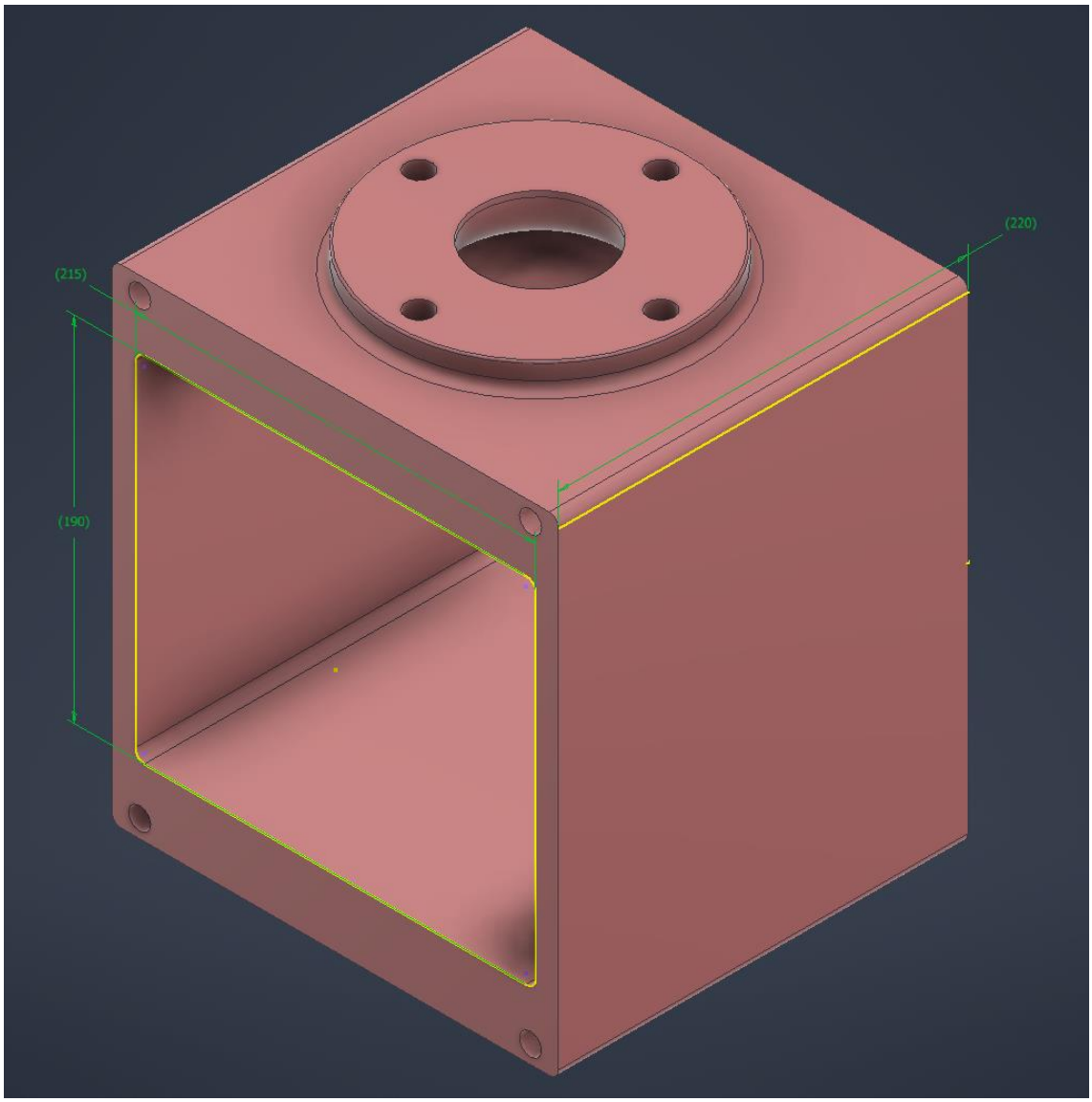

Figure 52. Final precooler dimensions.

Considering the increased requirement in power density, a mostly oval-tube array was chosen over a full airfoil geometry as seen in Figure 53. The reduction in intake flow velocity makes less efficient geometries more attractive, as pressure losses are roughly related to the square of flow velocity. The exterior walls were also included into the final

design, with “split” tubes shaping the inside walls of the precooler shell. Coolant circulation is designed so that the exterior walls are also cooled to maximize heat transfer surface area.

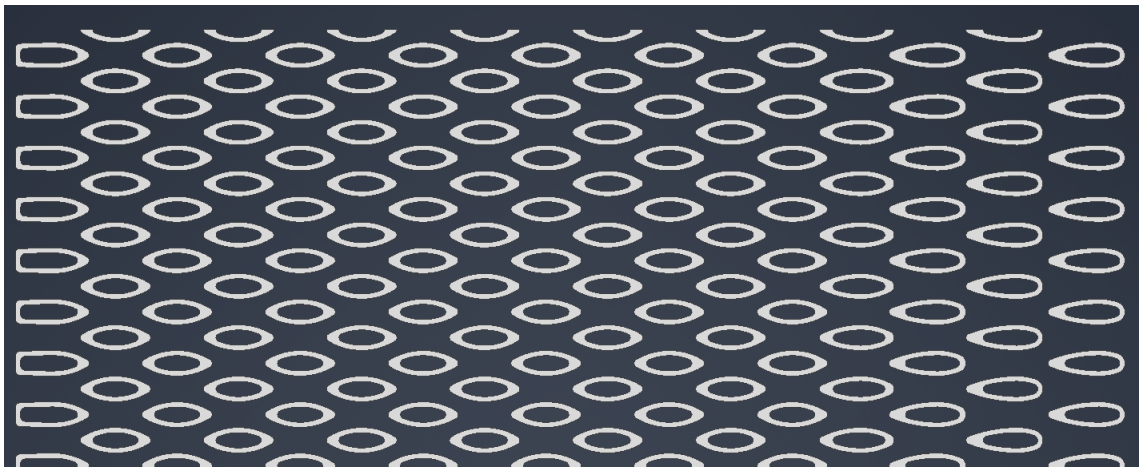

Figure 53. The chosen heat exchange geometry.

To reduce the pressure loss, the first few tube banks are shaped in an airfoil shape as demonstrated in Figure 54. This shape then morphs bank-by-bank to form the oval tubes which make up most of the array. This choice is further explored in section 3.3.1. Longitudinal spacing of these tubes was also altered to better match the ideal separation which was found to be roughly the chord length of each tube. As the oval tubes can have a shorter chord for a given thickness, longitudinal pitch must vary when transitioning from one shape to another. This kind of tube geometry modulation is made feasible by additive manufacturing. **Conventional manufacturing methods would see a large increase in cost if tube shape changes multiple times, while for additive manufacturing this is a non-issue**. This method opens another opportunity for optimization: tubes could change their shape also along each bank and not only from bank-to-bank. Indeed, each individual tube could be shaped separately, but this would only be feasible if the flow conditions are precisely known and enough design time can be afforded. Currently it is hard to estimate how much performance could be gained from such an endeavor, but it would most likely reduce the range of optimal flow conditions for the heat exchanger while providing better peak performance.

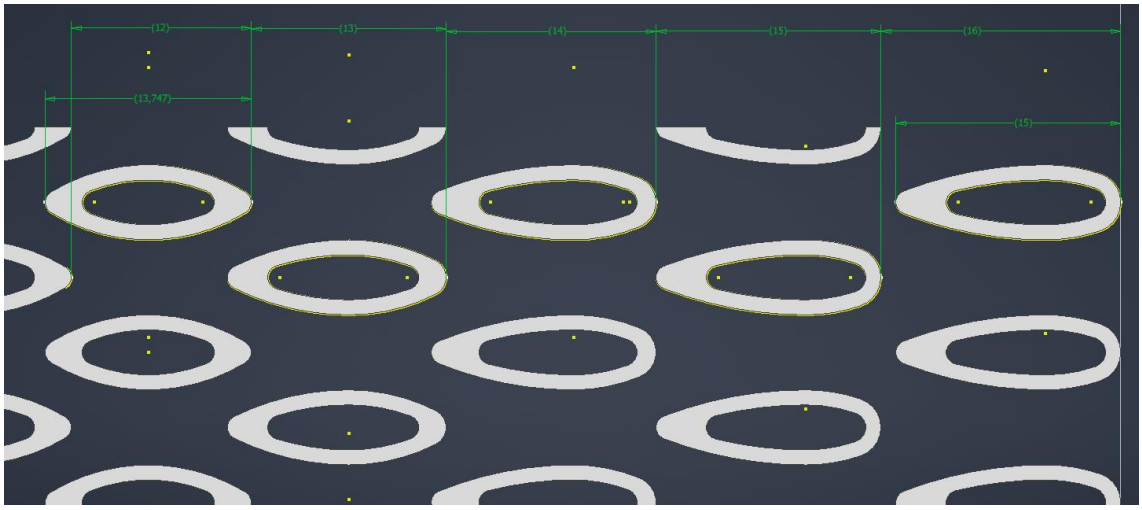

Figure 54. Detail and dimensions of the leading tube banks.

To estimate the performance of the full HX array, the ε-NTU method was employed once more with simulated input data. The final core, consisting of 366 tubes and weighing ~6 kg, was then compared to conventional high-performance heat exchange geometries from Kays & London (1984), and the existing charge air cooler when installed without a precooler. It should be noted that **no experimental data was available for any of these geometries in the operating conditions of the precooler** apart from the existing CAC, whose performance is well known. An extrapolation was made to account for the increased Reynold number for data from Kays & London, and simulated data was used for the oval-tube precooler. This means that there remains a large amount of uncertainty in the final performance estimations which will not be resolved until experimental data is available, either from a test bench or the engine in Wärtsilä's laboratory. This performance comparison is presented in table 6. Cases S1.5-1.25, S1.5-1.5 are unfinned round tubes, and cases CD-8.8-1.0-J(a) and CF-8.72(c) represent finned tubes at 2 area densities. The fin effectiveness is not accounted for, but it is around 98% for these geometries. Intake flow uniformity, or lack thereof, is likewise not taken into consideration apart from the existing CAC. Its performance numbers are derived from the running engine and thus have this factor built in.

Table 6. Performance estimations of designed and known heat exchange geometries.

Geometry	Area density [1/m]	j/f	Pressure loss [Pa]	Heat transfer rate [W]
Designed	243	0.126	3500	173 000
CAC	~320	0.003	1500	262 000
S1.5-1.25	176	0.114	7600	160 000

S1.5-1.5	147	0.116	7900	160 000
8.8-1.0-J(a)	300	0.141	3700	160 000
8.72(c)	446	0.119	3500	160 000

As seen in table 6, conventional finned heat exchange surfaces can provide the required performance for use in a precooler. These are however impractical to manufacture using powder-bed methods and are not as robust for intake flow variations as geometries with only primary heat transfer surfaces. Their performance at the operating conditions of the precooler also remains in question, especially when considering how comparatively poorly the existing CAC is performing. The heat exchange geometry of the CAC is close to case CD-8.8-1.0-J(a), though the exact core properties are not available. Nonetheless, the performance of the existing CAC suggests that finned geometries do not perform nearly as well under these conditions as experimental data would suggest. **It remains to be seen how well the newly designed precooler performs in the intended operating conditions**.

It is also fair to assume that the designed airfoil-tube geometry does not perform as well as the simulations suggest. This fact cannot be circumvented until experimental data becomes available at or near the operating conditions of the engine, and the simulation models used are tuned to provide results matching these experiments. As of writing, large margins of error remain the only option to ensure required performance. This however applies to any heat exchanger, not only those designed with CFD.

4 CONCLUSIONS

In this work, an air-to-water heat exchanger was designed to support an existing charge air cooler for a Wärtsilä W6L20CR-DF internal combustion engine. The design work was carried out using OpenFOAM -CFD tools and the resultant geometry will be manufactured using a selective laser melting process. The geometry chosen is a non-finned airfoil- and oval-shaped tube array. Secondary surfaces i.e. fins were deemed impractical for additive manufacturing and thus only primary surfaces were used. These surfaces were then optimized using computational fluid dynamics to meet the demanding performance criteria. This choice of surface geometry is not the only geometry that can provide the required performance, but it is efficient and conducive to additive manufacturing. Clear development and optimization path can be seen for future work, with for example individual tube optimization and more refined conformal design of the whole array.

Heat exchanger design has conventionally been an art of extrapolating tabulated experimental data to each application at hand. This method has proven to work very well, as is demonstrated by well-performing heat exchangers all around us. However, for applications in extreme operating conditions, or under unconventional geometric constrains, this methodology may falter unless augmented with experimentation at the specific conditions. This becomes a major issue when combined with the possibilities of additive manufacturing, as suddenly the space of possible geometries is vastly increased. Conventional heat exchange geometries are also unattractive for use in AM applications for various reasons. This means that there remains a large open area of research and application for future engineering work on the subject. Majority of the current research seems to lie in microscale heat exchangers, but as this work demonstrates, also macroscale applications can benefit from use of additive manufacturing techniques.

Additive manufacturing can certainly be used to create effective heat exchangers. Its limitations (currently) lie in manufacturing cost and lack of established design practices. Each custom AM HX is more expensive than an off-the-shelf solution, but the costs of AM are expected to come down as time progresses. The lack of design practices is therefore a more pressing issue. As AM allows for a near unlimited possibilities in heat exchange surface geometries, conventional empirism and data tabulation becomes unfeasible. Furthermore, one of the advantages of AM heat exchangers is the ability to

design them in a conformal way for each use case, i.e. not just in common shapes and sizes like commercial HX: s, but specifically tailored for every application. This can be considered as the key advantage of AM in HX design. Conventional heat exchangers will however remain an attractive option, as they are well-understood, economical and easily available. AM HX: s should be employed where they provide the most benefit: under difficult geometric and performance constrains and small production volumes.

To take advantage of the possibilities opened by additive manufacturing, computational fluid dynamics is a natural choice to analyze and improve HX designs. CFD will most likely become an extremely important tool in AM HX design, especially considering the improvements in software and hardware that we see year over year. However, there remains a large need for future work in validating CFD-models experimentally for the application of interest. The need for experimental validation is nothing new in the field of simulation and is something that large enterprises like Wärtsilä should be able to achieve quite easily. The wide range of use cases seen for large internal combustion engines is a perfect fit for additively manufactured heat exchangers.

SOURCES

Al-Ketan O., Ali M., Khalil M., Rowshan R., Khan K.A., Abu Al-Rub R.K., 2020. Forced Convection Computational Fluid Dynamics Analysis of Architected and Three-Dimensional Printable Heat Sinks Based on Triple Periodic Minimal Surfaces. Thermal Science and Engineering Applications, 13(2): 021010

Bacellar D., Aute V., Huang Z., Radermacher R., 2017. Design optimization and validation of high-performance heat exchangers using approximation assisted optimization and additive manufacturing. Science and Technology for the Built Environment, 23 (2017), P. 896-911

Fiebig M., 1998. Vortices, Generators and Heat Transfer. Chemical Engineering Research and Design, Vol. 46(2), P. 108-123

Ho J.Y., Wong K.K., Leong K.C., Wong T.N., 2017. Convective heat transfer performance of airfoil heat sinks fabricated by selective laser melting. International Journal of Thermal Sciences, 114 (2017), P. 213-228

Huang, K., Wan J.W., Chen C.X., Mao D.F., Li Y.Q., 2012. Experiments investigation of the effects of surface roughness on laminar flow in macro tubes. Experimental Thermal and Fluid Science, 45 (2013), P. 243-248

Incropera F.P., DeWitt D.P., 1985. Fundamentals of heat and mass transfer. New York: John Wiley & Sons, Inc., 802 p. ISBN 0-471-82561-1

Kaur, I., Singh P., 2021. State-of-the-art in heat exchanger additive manufacturing. International Journal of Heat and Mass Transfer, 178 (2021) 1216000

Kays, W. M. and London A. L., 1984. Compact heat exchangers, third edition. New York: McGraw-Hill, 335 p. ISBN 1-57524-060-2

Kokkonen P., Salonen L., Virta J., Hemming B., Laukkanen P., Savolainen M., Komi E., Junttila J., Ruusuvuori K., Varjus S., Vaajoki A., Kivi S., Welling J., 2016. Design guide for additive manufacturing of metal components by SLM process. VTT Technical Research Centre of Finland, VTT-R-03160-16

Kuppan, T., 2000. Heat Exchanger Design Handbook. New York: Marcel Dekker Inc, 1119 p. ISBN 0-8247-9787-6

Pyzybylski, M., 2021. Additional cooler for the W6L20CR-DF charge air system. Stage I Report. Vaasa: Wärtsilä, 145 p. DMTA00044405, internal release

Rastan H., Abdi A., Hamawandi B., Ignatowicz M., Meyer J.P., Palm B., 2020. Heat transfer study of enhanced additively manufactured minichannel heat exchangers. International Journal of Heat and Mass Transfer, 161 (2020) 120271

Saltzman, D., Bichnevicius M., Lynch S., Simpson T.W., Reutzel E.W., Dickmann C., Martukanitz R., 2018. Design and evaluation o an additively manufactured aircraft heat exchanger. Applied Thermal Engineering, 138 (2018), P. 254-263

Shah R.K., Sekulic D.P., 2003. Fundamentals of heat exchanger design. New York: John Wiley & Sons, Inc., 941 p. ISBN 978-0-471-32171-2

Stimpson, C.K., Snyder J.C., Thole K.A., Mongillo D., 2016. Roughness Effects on Flow and Heat Transfer for Additively Manufactured Channels. Journal of Turbomachinery, Vol. 138 / 051008

Ventola, L., Robotti F., Dialameh M., Calignano F., Manfredi D., Chiavazzo E., Asinari P., 2014. Rough surfaces with enhanced heat transfer for electronics cooling by direct metal laser sintering. International Journal of Heat and Mass Transfer, 75 (2014), P. 58-74

Wong M., Owen I., Sutcliffe C.J., Puri A., 2009. Convective heat transfer and pressure losses across novel heat sinks fabricated by Selective Laser Melting. International Journal of Heat and Mass Transfer, 52 (2009), P. 281-288